Microscopic Mechanisms and Dual Pathways of 5f Electron Itinerancy Tuned by Ligand Chemistry and Pressure in Paramagnetic Uranium Dipnictides

Reyhaneh Ebrahimi-Jaberi[1] and S. Jalali-Asadabadi[1,*]

[1]*Department of Physics, Faculty of Physics, University of Isfahan (UI), Hezar Jerib Avenue, Isfahan 8174673441, Iran*

The dual localized–itinerant character of uranium $5f$ electrons governs the electronic and magnetic properties of many actinide materials, yet the microscopic mechanisms controlling their tunable itinerancy remain incompletely understood. Here we investigate the uranium dipnictides UX_2 (X = P, As, Sb) using fully charge–self–consistent density functional theory combined with dynamical mean-field theory including spin–orbit coupling (SOC) in the paramagnetic (PM) state at $T = 300$ K. The calculations reveal that the uranium $5f$ shell resides in a mixed-valence configuration with occupancies $\langle n_{5f} \rangle \approx 2.6$–$2.8$, dominated by $5f^2$–$5f^3$ states. Momentum-resolved spectra and hybridization functions show that decreasing $5f$–p hybridization along the P → As → Sb series enhances correlation effects and strengthens $5f$ localization, whereas hydrostatic pressure increases hybridization and quasiparticle (QP) coherence, driving the system toward greater itinerancy. The Matsubara self-energy indicates coherent Fermi-liquid behavior at 300 K with pronounced spin–orbit–driven orbital differentiation, where the $j = 5/2$ manifold is more strongly renormalized than the $j = 7/2$ states. Local susceptibilities reveal sizable fluctuating $5f$ moments in the PM phase at room temperature, providing a qualitative—necessarily speculative—connection to magnetic scales inferred from previous static DFT calculations of the antiferromagnetic ground state. Additional calculations for UP_2 in its experimentally established tetragonal $I4/mmm$ phase show that the key features identified in the $P4/nmm$ reference structure—including the SOC-split $5f$ manifold, the dominance of $j = 5/2$ states near the Fermi level, and pressure-enhanced QP coherence—remain qualitatively preserved, with only moderate quantitative differences arising from the distinct crystallographic environment. Together these results establish a clear microscopic mechanism: ligand chemistry sets the baseline uranium–ligand hybridization and degree of $5f$ localization, while pressure continuously tunes the same control parameter, providing a unified framework for understanding how correlations, SOC, and hybridization govern $5f$ itinerancy in uranium intermetallic compounds.

I. INTRODUCTION

Actinide compounds exhibit a dual localized–itinerant character of $5f$ electrons that gives rise to heavy-fermion behavior, spin and valence fluctuations, unconventional superconductivity, and complex magnetic ordering [1–7]. The balance between localization and itinerancy governs magnetism and metallicity and can be tuned by chemical environment and thermodynamic variables such as temperature and pressure [8–10]. Ligand substitution is therefore an effective route to modify orbital hybridization and correlation strength [8].

Uranium dipnictides UX_2 (X = P, As, Sb) provide a platform to track the evolution of $5f$–p hybridization with ligand identity [11–15]. They are generally described by the tetragonal anti–Cu_2Sb–type structure ($P4/nmm$) [16, 17], although UP_2 adopts a more complex tetragonal $I4/mmm$ structure [18]. These compounds order antiferromagnetically at relatively high Néel temperatures, indicating strong exchange and significant $5f$–p mixing [16, 17]. Experiments reveal strong anisotropy, electron–lattice coupling, surface reconstructions relevant to spintronics, and pressure- and field-induced magnetic transitions reflecting the competition between localization and itinerancy [4, 12, 16, 19–26]. Spectroscopy and band-structure studies show that hybridized $5f$–p states dominate the low-energy electronic structure and Fermiology [13, 14, 27–32].

Despite this progress, the room-temperature paramagnetic (PM) phase of UX_2 remains insufficiently characterized. This regime is essential for revealing the intrinsic itinerant component of the $5f$ states without long-range order and for assessing how ligand identity and compression control metallicity and hybridization under technologically relevant conditions. Addressing these questions requires a framework able to capture thermal fluctuations, local-moment dynamics, and correlation-driven renormalizations with quantitative accuracy.

Static density-functional approaches within LDA or GGA, even when augmented with onsite corrections, miss key many-body dynamics and temperature dependence in $5f$ shells [33, 34]. Dynamical mean-field theory (DMFT) overcomes these limitations by treating local temporal fluctuations self-consistently [35, 36]. In the present work, we employ a fully charge self-consistent density functional theory (DFT) combined with embedded DMFT (DFT+embedded DMFT) framework to study UX_2 in the PM state at 300 K including spin–orbit coupling (SOC). Here, "embedded DMFT" refers to the self-consistent embedding of a local quantum impurity problem into the DFT electronic structure following the projector-based implementation of Haule and co-workers [34, 37, 38], and does not include frequency-dependent or nonlocal Coulomb interactions as in extended DMFT (EDMFT) formulations. For conciseness, we refer to this approach as DFT+DMFT throughout the remainder of the manuscript. The DFT part is performed using WIEN2k [39] with the PBE-GGA functional [39–42].

All DFT+DMFT calculations are performed for the $P4/nmm$ structure commonly used to describe the UX_2 se-

* Corresponding author: sjalali@sci.ui.ac.ir; saeid.jalali.asadabadi@gmail.com

ries. As an exception, Appendix B and Supplemental Material (SM) [43] also examine UP_2 in its experimentally reported tetragonal $I4/mmm$ structure [18] to test the robustness of the results against crystallographic details. The calculations are carried out in the PM phase at $T = 300$ K, above the Néel temperatures of UP_2, UAs_2, and USb_2 [16–18], where long-range magnetic order is absent, allowing the correlated metallic state of the uranium $5f$ electrons to be examined without symmetry breaking and enabling us to focus on how ligand substitution and hydrostatic pressure tune the balance between $5f$ localization and itinerancy.

Because earlier theoretical works [32, 44] on UX_2 have primarily focused on the antiferromagnetically ordered ground state within static DFT, it is useful to emphasize the distinction between those calculations and the present finite-temperature treatment. Static antiferromagnetic (AFM) DFT provides estimates of ordered moments and magnetic exchange scales at zero temperature, whereas the present DFT+DMFT calculations describe fluctuating local moments in the PM regime. Any comparison between these two descriptions should therefore be regarded as qualitative and necessarily speculative. Establishing a quantitative connection between the ordered and PM regimes would require a unified treatment of the AFM phase within the same DFT+DMFT framework.

This study reveals a concise and unified picture. At ambient pressure, replacing P with As and Sb does not produce a rigid shift of the U-$5f$ ($j = 5/2$) manifold away from the Fermi level (E_F). Instead, the low-energy $j = 5/2$ quasiparticle (QP) resonance remains pinned near E_F but becomes progressively narrower and more strongly renormalized across the series. The spectral weight at the E_F is reduced and redistributed, signaling enhanced mass renormalization and increased localization. This evolution reflects a systematic reduction of effective $5f$–p hybridization strength and a corresponding enhancement of correlation effects from UP_2 to USb_2. Hydrostatic pressure further enhances delocalization and strengthens conduction-state mixing, with a material-dependent response that is largest in UP_2 and weaker in UAs_2 and USb_2. Analysis of the density of states (DOS), the impurity hybridization function $\Im[\Delta(\omega)]$, and the momentum-resolved spectral function $A(\mathbf{k}, \omega)$ shows that ligand substitution is the primary control knob for itinerancy, while pressure acts as a precise fine-tuning parameter. The associated redistribution of $5f$ valence probabilities clarifies the microscopic origin: at zero pressure the trend toward enhanced localization correlates with increased $5f^3$ weight across P⟶As⟶Sb, whereas compression reduces $5f^3$ in favor of $5f^2$ and other itinerant configurations, enhancing charge fluctuations within the mixed-valence regime and strengthening QP coherence.

By establishing how ligand chemistry sets the baseline $5f$ itinerancy and how pressure refines it in the room-temperature PM phase, this study closes a key gap in the understanding of UX_2 and provides a predictive framework for tailoring actinide electronic structure for quantum, spintronic, and advanced electronic applications [1–17, 19–42].

II. THEORETICAL FRAMEWORK

A realistic description of uranium $5f$ electrons requires methods beyond static mean-field approximations such as LDA or GGA, which cannot capture dynamical correlations and local-moment fluctuations [33, 45]. We therefore employ a fully charge–self–consistent DFT+DMFT framework [34–36], in which the U $5f$ shell is treated as a correlated multi-orbital subspace embedded in the DFT electronic structure, including finite temperature and SOC.

DFT+DMFT combines DFT with a local dynamical self-energy obtained from an auxiliary quantum impurity problem [35, 36]. The formalism has been implemented in several electronic-structure platforms, including TRIQS-based interfaces [46] and RSPt [47].

In this work we use the fully charge–self–consistent implementation developed by Haule and collaborators [34, 38], interfaced with the WIEN2k all-electron DFT code [39]. The correlated subspace is constructed using projector-based embedding within a stationary Luttinger–Ward functional formulation, ensuring thermodynamic consistency and self-consistent feedback between the charge density and the local self-energy.

The physical conclusions reported here arise from the DFT+DMFT description of the UX_2 electronic structure and are therefore not tied to a specific software implementation, provided a fully charge–self–consistent multiorbital treatment is used.

A. Multiorbital DMFT formulation

Within DFT+DMFT, the correlated subspace (here the U $5f$ manifold with SOC) is defined through projectors that map the lattice Green's function onto its local counterpart,

$$\mathcal{G}_{mm'}(\omega) = \sum_{\mathbf{k}} P^{\dagger}_{m}(\mathbf{k})\, G_{\mathbf{k}}(\omega)\, P_{m'}(\mathbf{k}), \tag{1}$$

where m, m' label the correlated spin–orbital states.

The auxiliary impurity problem is formulated in the same multiorbital space, with Dyson equation

$$\mathcal{G}^{-1}(\omega) = (\omega + \mu)\mathbf{I} - \mathbf{E}_{\text{imp}} - \Sigma_{\text{imp}}(\omega) - \Delta(\omega), \tag{2}$$

where $\mathbf{E}_{\text{imp}}$ contains the crystal-field and SOC splittings, $\Sigma_{\text{imp}}(\omega)$ is the local self-energy, and $\Delta(\omega)$ describes the dynamical coupling to the environment. Although these expressions are written on the real axis, the CT-QMC solver operates on the Matsubara grid, $\omega \to i\omega_n$ with $\omega_n = (2n+1)\pi k_B T$, following Refs. [37, 48]. Working on the imaginary axis avoids analytic-continuation uncertainties during impurity solution.

To clarify the role of hybridization, it is useful to distinguish a formal non-interacting bath from the self-consistent DMFT hybridization. For a true Anderson impurity model,

$$\Delta_{\text{bare}}(\omega) = \sum_{\mathbf{k}} \mathbf{V}^{\dagger}_{\mathbf{k}} \left[(\omega + \mu)\mathbf{I} - \mathbf{H}^{\text{DFT}}_{\mathbf{k}}\right]^{-1} \mathbf{V}_{\mathbf{k}}, \tag{3}$$

where $\mathbf{H}_{\mathbf{k}}^{\mathrm{DFT}}$ (PBE-GGA here) is the lattice Hamiltonian and $\mathbf{V}_{\mathbf{k}}$ encodes the $5f$–ligand couplings. Equation (3) is therefore a formal projection of the non-interacting DFT bath onto the correlated subspace; it provides a convenient measure of the magnitude and orbital character of the underlying $5f$–ligand hybridization.

In DMFT, however, the hybridization entering the impurity solver is determined self-consistently from the interacting lattice Green's function [37, 48, 49]:

$$\Delta(\omega) = (\omega + \mu)\mathbf{I} - \mathbf{E}_{\mathrm{imp}} - \Sigma_{\mathrm{imp}}(\omega) - \mathcal{G}^{-1}(\omega), \tag{4}$$

with $\mathcal{G}(\omega)$ defined in Eq. (2). This self-consistent $\Delta(\omega)$ is the actual DMFT embedding function and incorporates the feedback of the interacting lattice environment on the $5f$ shell.

In this manuscript, Eq. (3) is used solely to analyze the bare orbital structure and strength of $5f$–ligand coupling through $\mathbf{V}_{\mathbf{k}}$, whereas Eq. (4) defines the effective hybridization entering the impurity solver. This distinction preserves the microscopic interpretation of hybridization trends while maintaining full consistency with the self-consistent DFT+DMFT framework.

B. Lattice Green's function and charge self-consistency

The interacting lattice Green's function is evaluated on the fermionic Matsubara grid $(i\omega_n)$ as [46]

$$\mathbf{G}_{\mathbf{k}}(i\omega_n) = \left[(i\omega_n + \mu)\mathbf{I} - \mathbf{H}_{\mathbf{k}}^{\mathrm{DFT}} - \Sigma^{\mathrm{emb}}(i\omega_n)\right]^{-1}, \tag{5}$$

where $\mathbf{H}_{\mathbf{k}}^{\mathrm{DFT}}$ is the DFT Hamiltonian and the embedded self-energy is

$$\Sigma^{\mathrm{emb}}(i\omega_n) = \mathbf{P}^{\dagger}\left(\Sigma_{\mathrm{imp}}(i\omega_n) - \Sigma_{\mathrm{DC}}\right)\mathbf{P}. \tag{6}$$

Here Σ_{imp} is the impurity self-energy, Σ_{DC} the double-counting correction, and $\mathbf{P}$ the projector between Bloch and correlated subspaces. Real-frequency spectral quantities are obtained by analytic continuation of the Matsubara data using the maximum entropy method [50].

Charge self-consistency is achieved by recomputing the electronic density from the interacting Green's function, and the resulting density is fed back into the DFT cycle, closing the outer charge-self-consistency loop of the fully charge-self-consistent DFT+DMFT scheme.

C. Spectral Quantities and Their Relation to Valence Statistics

Experimentally accessible observables are obtained from the real-frequency Green's function. Since the CT-QMC solver provides the self-energy on the Matsubara axis, real-frequency quantities are obtained via analytic continuation $i\omega_n \to \omega + i0^+$ using the maximum entropy method [50]. The lattice Green's function $\mathbf{G}_{\mathbf{k}}(\omega + i0^+)$ then yields the spectral function

$$A(\mathbf{k}, \omega) = -\frac{1}{\pi}\,\Im\ \mathrm{Tr}\ \mathbf{G}_{\mathbf{k}}(\omega + i0^+), \tag{7}$$

and the interacting DOS

$$A(\omega) = \frac{1}{N_{\mathbf{k}}}\sum_{\mathbf{k}} A(\mathbf{k}, \omega). \tag{8}$$

To relate spectral quantities to CT-QMC valence statistics, let p_Γ denote the probability of atomic eigenstate Γ with $5f$ occupancy N_Γ. The average occupancy and its fluctuation are

$$n_f = \sum_{\Gamma} N_\Gamma\, p_\Gamma, \qquad \delta n_f^2 = \sum_{\Gamma} N_\Gamma^2 p_\Gamma - n_f^2, \tag{9}$$

where δn_f^2 measures charge fluctuations.

The configurational participation ratio

$$\mathcal{P} = \left(\sum_{\Gamma} p_\Gamma^2\right)^{-1}, \tag{10}$$

and the impurity entropy

$$S_{\mathrm{imp}} = -k_B \sum_{\Gamma} p_\Gamma\ \ln p_\Gamma \tag{11}$$

characterize multiplet mixing and local many-body degeneracy.

Within fully charge–self-consistent DFT+DMFT, the impurity occupancy equals the lattice occupancy obtained from the spectral function. Thus n_f can equivalently be written as

$$n_f = \frac{1}{N_{\mathbf{k}}}\sum_{\mathbf{k}} \int_{-\infty}^{+\infty} d\omega\, f(\omega)\ \mathrm{Tr}\, A(\mathbf{k}, \omega), \tag{12}$$

where $f(\omega)$ is the Fermi–Dirac distribution.

Correlation effects are quantified by the QP renormalization factor

$$Z = \left[1 - \partial_\omega \mathrm{Re}\,\Sigma(\omega)\big|_{\omega=0}\right]^{-1}, \qquad \frac{m^*}{m} = Z^{-1}, \tag{13}$$

which relates the low-frequency self-energy to mass enhancement. In practice, Z is extracted from the Matsubara-axis self-energy $\Im[\Sigma_j(i\omega_n)]$ for numerical stability, as given in Eq. (A3) and discussed in Appendix A AV.

Orbital-resolved spectral functions projected onto the correlated $5f$ manifold are defined as

D. Implementation for UX_2

In this study the uranium $5f$ shell (including SOC) defines the correlated subspace. The multiorbital impurity problem of Eq. (2) is solved using continuous-time quantum Monte Carlo (CT-QMC) at $T = 300$ K within fully charge–self–consistent calculations. Additional details on projector construction, numerical convergence, and pressure implementation are given in Sec. III and Appendix A.

TABLE I. Comparison of uranium magnetic quantities for PM and AFM phases of UX_2 (X = P, As, Sb), in units of μ_B per U atom. The PM DFT+DMFT values obtained in the present work (marked by *) correspond to the root-mean-square longitudinal local moment $\mu_{\mathrm{loc},z} = \sqrt{\langle \hat{m}_z^2 \rangle}$ evaluated at $T = 300$ K. The experimental PM values are effective moments extracted from susceptibility measurements over the indicated temperature ranges, whereas the AFM values from earlier DFT and experimental studies correspond to static ordered moments. Temperatures (T) are given in Kelvin. The symbol "–" indicates data not available (N/A) or not specified, and blank cells denote repetition of the entry in the row above.

System	Method	Magnetic Phase	XC Scheme	SOC	μ_U (μ_B)	T (K)	Ref.
UP_2	DFT+DMFT	PM	PBE-GGA	Yes	2.410	300	*
	DFT	AFM	WC-Fock		1.274	0	[32]
			PBE-GGA+U ($U_{\mathrm{eff}} = 0.29$ Ry)	No	1.76	0	[44]
	Exp.	PM	–		2.50	210–450	[16]
		AFM	–		2.0 ± 0.1	–	[16]
UAs_2	DFT+DMFT	PM	PBE-GGA	Yes	2.328	300	*
	DFT	AFM	WC-Fock		1.645	0	[32]
			PBE-GGA		0.9 ± 0.01	–	[8]
			LDA+U ($U_{\mathrm{eff}} = 0.15$ Ry)	No	1.61	0	[44]
	Exp.	PM	–		2.94	300–410	[16]
		AFM	–		1.61 ± 0.11	–	[16]
USb_2	DFT+DMFT	PM	PBE-GGA	Yes	2.263	300	*
	DFT	AFM	WC-Fock		2.223	0	[32]
			PBE-GGA		0.7 ± 0.01	–	[8]
			LDA+U ($U_{\mathrm{eff}} = 0.22$ Ry)	No	1.83	0	[44]
	Exp.	PM	–		3.04	220–400	[16]
		AFM	–		1.88 ± 0.03	–	[16]

III. COMPUTATIONAL FRAMEWORK

Fully charge self-consistent DFT+DMFT calculations are performed for UX_2 (X = P, As, Sb) in the PM state at $T = 300$ K. The DFT part is carried out with WIEN2k using the FP-APW+lo basis [39–41, 51] and the PBE-GGA exchange–correlation functional [42]. Local dynamical correlations on the U-5f shell are treated within embedded DMFT [34, 35, 38], including SOC throughout. Experimental tetragonal anti-Cu_2Sb structures are used as starting geometries [13, 16], and calculations are performed in the PM state consistent with room-temperature behavior [16].

Kohn–Sham equations are solved on Monkhorst–Pack meshes (typically $18 \times 18 \times 8$) with standard WIEN2k convergence parameters [52, 53]. The impurity problem is solved using CT-QMC within the DFT+DMFT implementation [54–56], employing nominal double counting [34, 57, 58]. Interaction parameters $U = 4$ eV and compound-dependent J values (~ 0.595 eV) are used for the U-5f shell. DOS and $A(\mathbf{k}, \omega)$ are obtained from analytically continued self-energies using the maximum entropy method [50]; denser meshes (up to $27 \times 27 \times 13$) are used for final spectra.

Hydrostatic compression is simulated by uniformly scaling the optimized zero-pressure tetragonal unit cell while keeping its optimized zero-pressure c/a ratio fixed. The pressure associated with each sampled volume is obtained by fitting the calculated total-energy–volume data to the third-order Birch–Murnaghan equation of state [59]. Representative EOS-calibrated compression points of 4.427, 5.300, and 8.721 GPa are considered for UP_2, UAs_2, and USb_2, respectively. These values are EOS-derived pressures associated with the selected sampled volumes rather than independently prescribed target pressures. Additional technical settings, convergence thresholds, and validation checks concerning the projectors, embeddings, and charge-self-consistency cycles are provided in Appendix A.

IV. RESULTS AND DISCUSSIONS

A. Evolution of the local uranium moment across UX_2

Table I compares uranium magnetic quantities for UX_2 (X = P, As, Sb) obtained in the present PM DFT+DMFT calculations with available experimental data and with AFM ordered moments reported in earlier DFT studies [32, 44]. This comparison is intended to place the present PM DFT+DMFT results on the same overall magnetic scale as experimentally inferred paramagnetic moments and previously reported ordered AFM moments, while keeping clear that these quantities are not identical observables. The PM DFT+DMFT values reported here are equal-time local fluctuation amplitudes evaluated at $T = 300$ K, the experimental PM values are effective moments extracted from Curie–Weiss fits over finite temperature windows, and the AFM entries correspond to static ordered moments in symmetry-broken states, typically at or near zero temperature.

In the paramagnetic phase, the thermally averaged on-site magnetization vanishes, $\langle \hat{m}_z \rangle = 0$, but this does not imply the absence of local magnetism. In a correlated uranium

$5f$ shell, sizable instantaneous moments remain present and manifest themselves through finite local fluctuations. Within DFT+DMFT, these fluctuations are obtained from the impurity density matrix ρ generated by the CT-QMC solver. The statistical weight of a local many-body eigenstate $|i\rangle$ is

$$p_i = \langle i|\rho|i\rangle, \tag{14}$$

where the states $|i\rangle$ are eigenstates of the local impurity Hamiltonian including the Coulomb interaction, Hund's coupling, tetragonal crystal-field splitting, and spin-orbit coupling (SOC). Because SOC is treated fully relativistically, these states are generally not pure atomic $|LSJ\rangle$ multiplets, but contain mixtures of different LS terms and different $5f$ occupancies. The PM impurity ensemble is therefore a statistical mixture of many-body configurations with mixed atomic character rather than a single multiplet with a unique Landé factor.

For reference, one may characterize local angular-momentum fluctuations through

$$J_{\rm loc} = \sqrt{\langle \hat{\mathbf{J}}^2\rangle} = \sqrt{\mathrm{Tr}\left(\rho\,\hat{\mathbf{J}}^2\right)} = \sqrt{\sum_i p_i\langle i|\hat{\mathbf{J}}^2|i\rangle}, \tag{15}$$

with $\hat{\mathbf{J}} = \hat{\mathbf{L}} + \hat{\mathbf{S}}$. In tetragonal symmetry this fluctuation may be decomposed as

$$\langle \hat{\mathbf{J}}^2\rangle = \langle \hat{J}_z^2\rangle + \langle \hat{J}_x^2\rangle + \langle \hat{J}_y^2\rangle \equiv \langle \hat{J}_\parallel^2\rangle + 2\langle \hat{J}_\perp^2\rangle, \tag{16}$$

where $\hat{J}_\parallel \equiv \hat{J}_z$ is the component along the crystallographic c axis. However, the magnetic moment listed in Table I is not obtained by converting $J_{\rm loc}$ into a moment through an assumed effective Landé factor. For an isolated atomic $|LSJ\rangle$ multiplet one has the identity

$$\hat{\mathbf{L}} + 2\hat{\mathbf{S}} = g_J\hat{\mathbf{J}}, \tag{17}$$

with g_J given by the standard Landé formula, as recalled in the Supplemental Material of Ref. [60]. In the present DMFT impurity problem, by contrast, the density matrix samples a many-body ensemble with different occupancies and mixed atomic character, so no unique multiplet-specific g_J can be assigned to the full ensemble.

For this reason, and in direct response to the question of how the PM moment is evaluated, the local magnetic moment in the paramagnetic phase is measured directly from the magnetic-moment operator itself,

$$\hat{m}_z = -\mu_B(\hat{L}_z + 2\hat{S}_z), \tag{18}$$

in the local coordinate frame aligned with the crystallographic axes. The fluctuating longitudinal local moment reported in Table I is then defined as

$$\mu_{{\rm loc},z} = \sqrt{\langle \hat{m}_z^2\rangle} = \sqrt{\mathrm{Tr}\left(\rho\,\hat{m}_z^2\right)} = \mu_B\sqrt{\sum_i p_i\left\langle i\left|(\hat{L}_z + 2\hat{S}_z)^2\right|i\right\rangle}. \tag{19}$$

Accordingly, the PM DFT+DMFT entries in Table I are not obtained from a measured value of $\langle J\rangle$ or from $J_{\rm loc}$ by postulating a fixed g_J. Instead, they represent the root-mean-square longitudinal on-site magnetic-moment fluctuation of the correlated uranium $5f$ shell. This definition preserves the operator content of Eq. (17) where appropriate, while avoiding the unjustified reduction of the full relativistic many-body ensemble to a single effective atomic multiplet.

This distinction is essential for the interpretation of Table I. The calculated PM DFT+DMFT moments, $\mu_{{\rm loc},z} = 2.410$, 2.328, and 2.263 μ_B for UP_2, UAs_2, and USb_2, respectively, are of the same overall magnetic scale as the experimental paramagnetic effective moments, but they do not reproduce the same monotonic trend across the UX_2 series. This is not an inconsistency, because the experimental PM values are inferred from thermodynamic susceptibility fits over finite temperature ranges, whereas Eq. (19) defines an equal-time local impurity observable evaluated at fixed temperature. The two quantities probe related local magnetic physics, but they are not identical observables and are not expected to coincide quantitatively on a compound-by-compound basis.

The evolution of $\mu_{{\rm loc},z}$ across UX_2 must therefore be interpreted together with the broader set of DFT+DMFT indicators of itinerancy, screening, and localization. Table II summarizes two complementary local quantities in the PM phase, namely the average $5f$ occupancy $\langle n_{5f}\rangle$ and the local magnetic susceptibility $\chi_{\rm loc}$. Within DMFT, the local susceptibility $\chi_{\rm loc}$ defined in Eq. (20) measures the strength of dynamical local-moment fluctuations on the uranium site. All three compounds lie in an intermediate-valence regime, with $\langle n_{5f}\rangle = 2.64$–$2.82$, consistent with the mixed $5f^2/5f^3$ character discussed in Sec. II C. At ambient pressure, $\langle n_{5f}\rangle$ increases from 2.67 in UP_2 to 2.73 in UAs_2 and 2.82 in USb_2, indicating a progressive shift toward a more localized $5f^3$-like state. The trend in $\chi_{\rm loc}$ is even more pronounced, rising from 61.88 to 86.36 and then to 125.99 across the same sequence. This demonstrates that ligand substitution affects dynamical screening more strongly than it changes the average occupancy itself.

These local trends are fully consistent with the one-particle spectral and hybridization data. As discussed in Sec. IV C, the low-energy hybridization is progressively reduced from P to As to Sb, as seen in Fig. 2. The total and projected spectral functions in Fig. 1 show that the U-$5f$ weight near E_F becomes more narrowly concentrated and less strongly hybridized with ligand states along the series, while the momentum-resolved spectra in Fig. 3 display less dispersive low-energy quasiparticle features from UP_2 to USb_2. These trends all point to weaker bath coupling and more localized uranium-$5f$ character as the ligand is changed from P to Sb.

The same conclusion follows from the self-energy and valence-state diagnostics. The Matsubara self-energies in Fig. 4 show a systematic increase in the low-frequency slope of $\Im[\Sigma_j(i\omega_n)]$, particularly in the $j = 5/2$ sector that dominates the low-energy physics. Through Eq. (A3), this implies a reduced quasiparticle weight and stronger mass renormalization from UP_2 to UAs_2 to USb_2. At the same time, the valence-state probabilities in Fig. 5 show an increasing statistical weight of the dominant $5f^3$ configuration across the series, again indicating a gradual shift toward a more correlated and localized uranium configuration. Taken together, the reduced hybridization, enhanced self-energy renormalization, larger $\chi_{\rm loc}$, larger $\langle n_{5f}\rangle$, and increasing $5f^3$ weight establish a coherent and internally consistent picture of stronger correlation and localization from P to As to Sb.

Within this broader context, the slight decrease of the longitudinal fluctuation amplitude $\mu_{{\rm loc},z}$ from UP_2 to UAs_2 to USb_2 should not be interpreted as contradicting the localization trends extracted from the other observables. In a relativistic tetragonal many-body system, $\mu_{{\rm loc},z}$ is a component-resolved equal-time fluctuation amplitude rather than a unique scalar measure of correlation strength. Its value can be affected by the redistribution of statistical weight among SOC- and crystal-field-entangled many-body configurations, as well as by changes in the balance between longitudinal and transverse fluctuation channels [cf. Eq. (16)], even while the overall electronic state becomes more localized. Thus, stronger correlations do not require that every individual fluctuation component increase monotonically. In the present case, the weak monotonic reduction of $\mu_{{\rm loc},z}$ is best understood as a subtle reorganization of the local fluctuation channels within the correlated PM state, not as evidence against the robust localization trend established collectively by Table II and Figs. 1–5.

Hydrostatic pressure produces the opposite tendency within each compound and therefore provides a useful internal consistency check. As shown in Table II, the $5f$ occupancy decreases slightly under compression, by about 0.02–0.03, while $\chi_{\rm loc}$ is reduced more substantially, by 12.3% in UP_2, 13.1% in UAs_2, and 7.0% in USb_2. The modest change in $\langle n_{5f}\rangle$ shows that pressure does not alter the overall intermediate-valence character, but the stronger suppression of $\chi_{\rm loc}$ indicates enhanced screening and weaker local-moment fluctuations. This is consistent with the pressure evolution of the hybridization function in Fig. 2, the sharpening of low-energy spectral features in Fig. 3, and the reduction of the low-frequency self-energy slope in Fig. 4, all of which point to stronger quasiparticle coherence and a more itinerant low-energy state under compression.

It is equally important to distinguish the PM fluctuation moment discussed above from the AFM ordered moments listed in Table I. The AFM values from earlier DFT calculations and experiment characterize static ordered moments in symmetry-broken magnetic states, whereas the PM DFT+DMFT values and experimental Curie–Weiss moments describe fluctuating local moments in a correlated paramagnetic regime. These quantities are therefore distinct observables. They may be compared at the level of overall magnetic scale and systematic trends, but they are not expected to coincide quantitatively. In particular, the fact that AFM ordered moments are often smaller than PM effective or PM fluctuation moments should not be interpreted as a consequence of suppressing dynamical fluctuations in a way that directly increases or decreases the static moment. Rather, it reflects the comparison of different magnetic quantities defined in different physical regimes and extracted by different theoretical or experimental procedures.

Accordingly, the most robust conclusion from the present DFT+DMFT analysis is not a one-to-one numerical correspondence between all PM and AFM entries in Table I, but a coherent physical picture of how uranium $5f$ magnetism evolves across the UX_2 series. Ligand substitution from P to As to Sb progressively weakens low-energy hybridization, enhances self-energy renormalization, increases $\chi_{\rm loc}$, shifts the valence distribution toward stronger $5f^3$ character, and thereby drives the uranium $5f$ shell toward a more correlated and localized regime. Within that same relativistic many-body state, the directly measured longitudinal RMS fluctuation moment $\mu_{{\rm loc},z}$ shows a slight decrease, reflecting a redistribution of fluctuation channels rather than a reduction of overall correlation strength. A fully self-consistent AFM DFT+DMFT treatment would be required to track, on the same theoretical footing, the evolution from the PM fluctuating local-moment regime to the symmetry-broken AFM ordered state, which lies beyond the scope of the present work.

Details of the paramagnetic local-moment calculation are given in Sec. SMVI and summarized in the flowchart presented in Fig. SM4 of the SM.

B. Electronic duality and tunable itinerancy in SOC–resolved U–5f states of UX_2 (X = P, As, Sb)

Figure 1 shows the total and projected DOSs of UX_2 in the PM phase at T = 300 K obtained from fully charge self-consistent DFT+DMFT including SOC. All compounds exhibit finite spectral weight at the E_F, consistent with metallic behavior.

The low-energy window around E_F is dominated by U–$5f$ states, whereas ligand–p and U–$6d$ states mainly occupy deeper bonding energies (approximately −6 to −0.5 eV for UP_2, −6 to −0.7 eV for UAs_2, and −6 to −1.5 eV for USb_2). Transport and low-energy magnetic properties are therefore primarily governed by the $5f$ manifold, with p and d states providing hybridization channels.

SOC splits the U–$5f$ shell into $j = 5/2$ and $j = 7/2$ sublevels [panels (a_4–a_5, b_1)]. The $j = 5/2$ component forms a narrow resonance at E_F and controls coherent transport, while the broader $j = 7/2$ weight lies at higher energy. At ambient pressure, a clear chemical trend is observed: along P⟶As⟶Sb the low-energy $j = 5/2$ spectral weight decreases and the QP peak becomes less pronounced. This behavior is consistent with increasing U–X bond length across the series and reduced effective p–f hybridization, leading to enhanced $5f$ localization toward USb_2.

Hydrostatic compression (4.43 GPa for UP_2, 5.3 GPa for UAs_2, and 8.72 GPa for USb_2; Sec. A AII) enhances the DOS at E_F in all compounds [panels (b_2–b_4)]. The dominant peaks adjacent to E_F shift toward the E_F, and spectral weight is redistributed into the low-energy $j = 5/2$ resonance. The pressure response is strongest in UP_2 and weakest in USb_2, reflecting the larger hybridization change in the more itinerant member of the series.

Orbital-resolved DOSs show that pressure mainly reshapes the U–$5f$ states within a few hundred meV of E_F, while deeper ligand–p and U–$6d$ features are only moderately af-

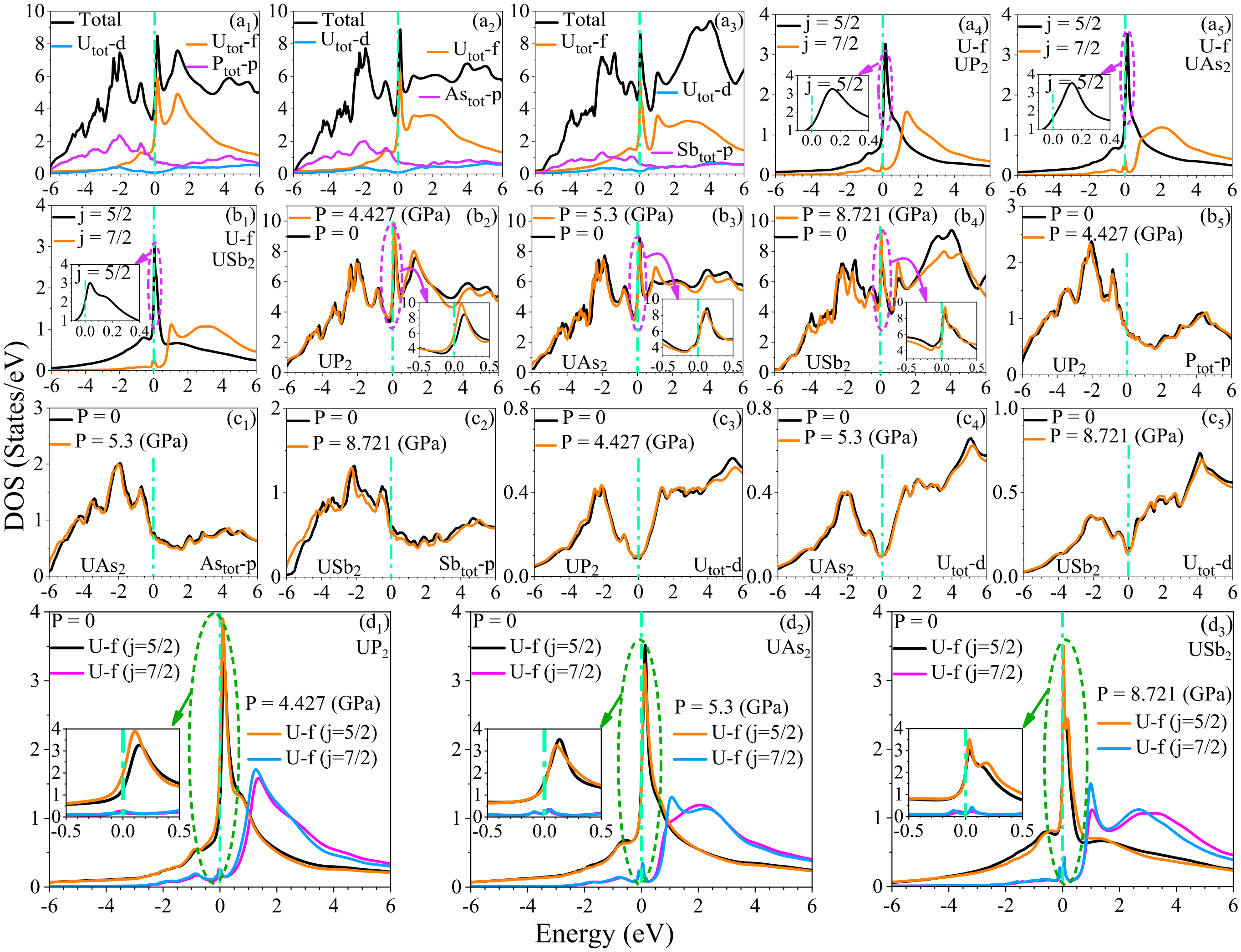

FIG. 1. Total and projected DOSs for UX_2 (X = P, As, Sb) calculated within fully charge self-consistent DFT+DMFT including SOC. Panels (a_1–a_3) show total and orbital-resolved DOSs at ambient pressure. Panels (a_4–a_5, b_1) resolve the U–$5f$ manifold into $j = 5/2$ and $j = 7/2$ components. Panels (b_2–b_4) compare total DOS at ambient pressure (black) and under applied pressure (orange). Panels (b_5, c_1–c_2) and (c_3–c_5) show pressure-dependent X–p and U–d projected DOSs. Panels (d_1–d_3) display the pressure evolution of the U–$5f$ spectral weight. Vertical dashed–dotted lines denote E_F; insets magnify the low-energy region.

fected. The $j = 5/2$ sublevel is more pressure-sensitive than $j = 7/2$, reinforcing its central role in conduction. At higher energies (1–6 eV), compression redistributes unoccupied spectral weight within the conduction region, further modifying the coupling between conduction states and the $5f$ manifold.

Overall, ligand substitution from P to As to Sb reduces the effective $5f$–p hybridization and increases localization, whereas hydrostatic pressure enhances hybridization and itinerancy within each compound. In all cases, the low-energy electronic structure is governed by the $j = 5/2$ submanifold and by the redistribution of spectral weight near E_F.

These trends are quantified below through the imaginary part of the hybridization function, $\Im[\Delta(\omega)]$, which directly measures the coupling between U–$5f$ states and the itinerant bath within DFT+DMFT.

C. Pressure evolution of the U–$5f$ hybridization channels

Figure 2 shows the imaginary part of the symmetry-reduced U–$5f$ hybridization channels, $-\Im[\Delta_a^{\mathrm{avg}}(\omega)]$, for the SOC-resolved $j = 5/2$ and $j = 7/2$ manifolds. These quantities are obtained from the matrix-valued impurity hybridization function $\Delta(\omega)$ by grouping symmetry-equivalent components and averaging them within each channel, as described in Sec. SMV and illustrated in the flowchart presented in Fig. SM3 of the SM. The curves shown in Fig. 2 therefore do not represent the full hybridization matrix itself, but reduced channel-resolved measures of the dynamical coupling between the correlated U–$5f$ shell and the itinerant bath.

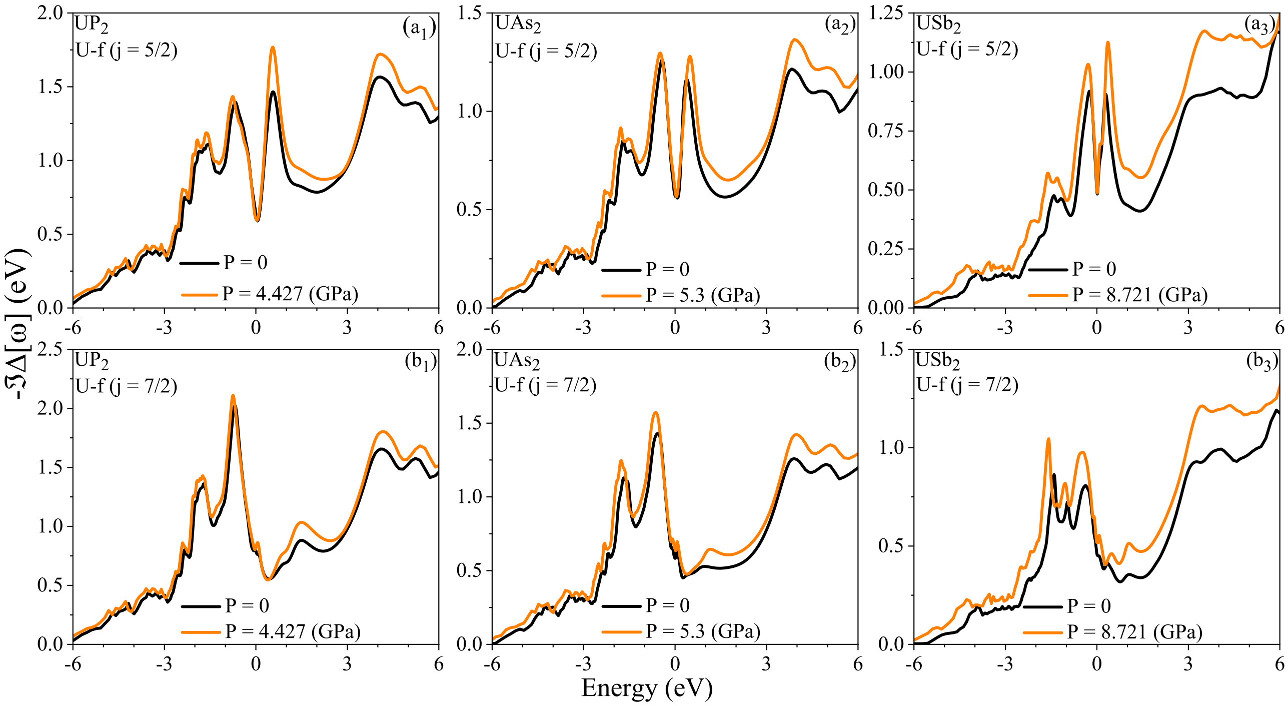

FIG. 2. Imaginary part of the symmetry-reduced impurity hybridization channels, $-\Im[\Delta_a^{\rm avg}(\omega)]$, for U–$5f$ states in UX_2 (X = P, As, Sb) from fully charge-self-consistent DFT+DMFT including SOC. Panels (a_1)–(a_3) show the $j = 5/2$ channels, and panels (b_1)–(b_3) the $j = 7/2$ channels. The plotted quantities are channel-resolved averages derived from the matrix-valued hybridization function $\Delta(\omega)$, as defined in Sec. SMV of the SM. Black curves denote ambient pressure, and orange curves denote hydrostatic compression (4.427, 5.3, and 8.721 GPa for UP_2, UAs_2, and USb_2, respectively).

For all three compounds, hydrostatic compression increases the hybridization channels over substantial parts of the energy range, including the low-energy region around E_F and parts of the occupied manifold below E_F. This overall enhancement indicates stronger $5f$–ligand coupling under compression and is consistent with the expected increase in orbital overlap as the lattice volume is reduced.

The detailed pressure response, however, is not uniform across compounds or across the two relativistic manifolds. In the $j = 5/2$ sector [Figs. 2(a_1)–(a_3)], the pressure-induced changes are clearly energy dependent, and the visual separation between the ambient- and high-pressure curves is not simply ordered as $UP_2 > UAs_2 > USb_2$ over the full spectral range. In particular, USb_2 shows a pronounced pressure-induced increase over broad positive energies in the $j = 5/2$ channel, whereas UP_2 exhibits strong modifications concentrated more strongly in the vicinity of the central spectral structures. The same caution applies to the $j = 7/2$ sector [Figs. 2(b_1)–(b_3)], where all three compounds respond to compression, but with different line-shape changes and different energy windows of strongest enhancement.

Accordingly, Fig. 2 supports a robust qualitative conclusion rather than a simple compound-by-compound scalar ranking: pressure strengthens the U–$5f$ hybridization channels throughout the UX_2 series, but the magnitude and spectral distribution of this enhancement are manifold dependent and material specific. For this reason, we avoid assigning a universal hierarchy of pressure response directly from Fig. 2, especially because the applied pressures differ among UP_2, UAs_2, and USb_2.

Because the impurity hybridization function enters directly into the impurity Dyson equation [Eq. (2)], the pressure-induced enhancement of $-\Im[\Delta_a^{\rm avg}(\omega)]$ implies stronger dynamical coupling between the correlated shell and its electronic environment. This trend is consistent with the broader pressure evolution found elsewhere in our DFT+DMFT results, including enhanced quasiparticle coherence, increased Z [Eqs. (13) and (A3)], reduced effective mass $m^*/m = Z^{-1}$, reduced impurity entropy $S_{\rm imp}$ [Eq. (11)], and increased charge fluctuations δn_f^2 [Eq. (9)].

We therefore interpret Fig. 2 as direct evidence that hydrostatic compression reinforces the dynamical U–$5f$–bath coupling in all three UX_2 compounds, while the spectral form of the response remains dependent on both the material and the relativistic manifold.

D. Pressure– and ligand–dependent evolution of the momentum–resolved spectral function

Figure 3 presents the momentum-resolved spectral function $A(\mathbf{k}, \omega)$ obtained from the lattice Green's function [Eq. (5)]. These spectra provide the $\mathbf{k}$-resolved counterpart to the local quantities discussed previously, including

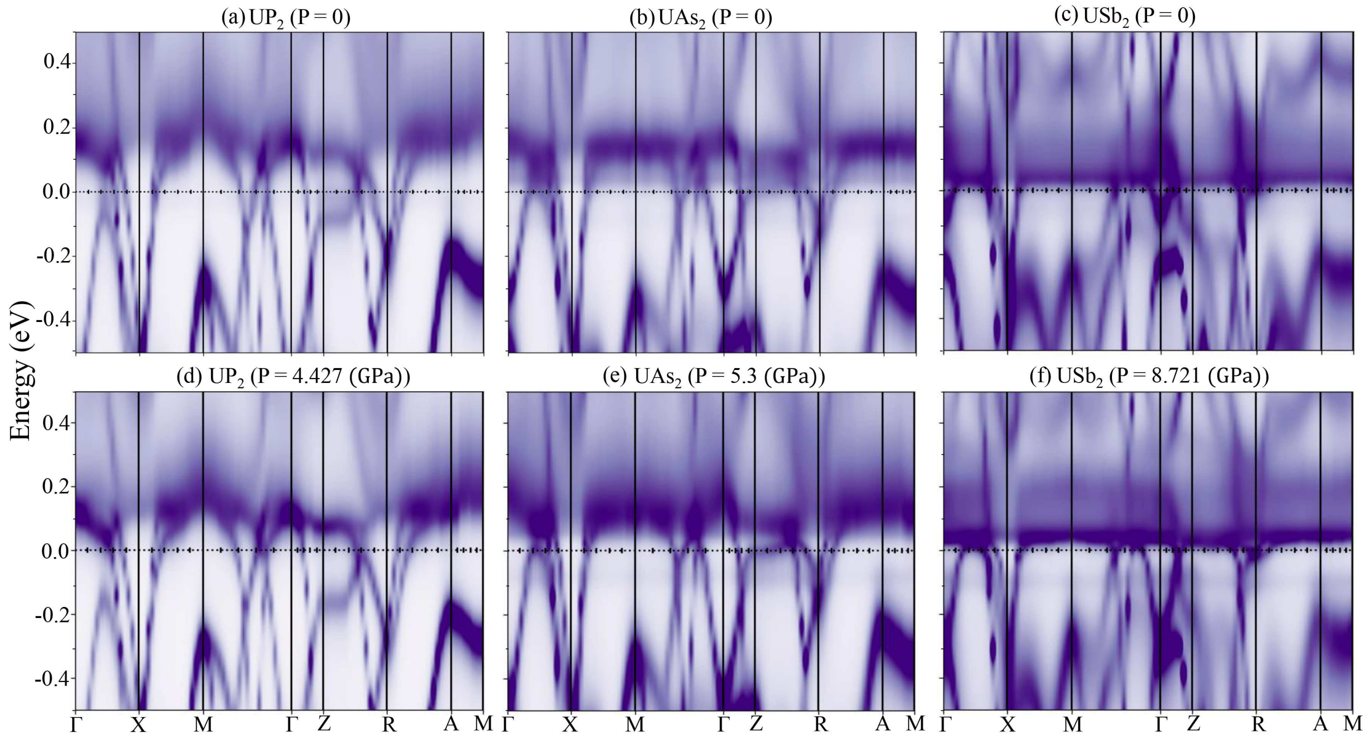

FIG. 3. Momentum-resolved spectral function $A(\mathbf{k},\omega)$ of UX_2 (X = P, As, Sb) from fully charge–self–consistent DFT+DMFT including SOC. (a)–(c): ambient pressure. (d)–(f): hydrostatic compression (4.427, 5.3, and 8.721 GPa for UP_2, UAs_2, and USb_2, respectively). High-symmetry path: Γ–X–M–Γ–Z–R–A–M–Γ. The dashed horizontal line marks E_F.

$-\Im[\Delta(\omega)]$ (Fig. 2) and the valence-state probabilities (Fig. 5).

At ambient pressure [Figs. 3(a–c)], all compounds display dispersive bands crossing E_F, confirming their metallic character. The low-energy intensity is dominated by U–$5f$ states split by SOC into $j = \frac{5}{2}$ and $j = \frac{7}{2}$ components. The $j = \frac{5}{2}$ manifold forms the coherent features near E_F, whereas the $j = \frac{7}{2}$ weight appears at higher binding energies and is less dispersive. Across the series P⟶As⟶Sb, the near-E_F bands become progressively narrower and more strongly renormalized, consistent with the reduction of $5f$–p hybridization identified in Sec. IV C. UP_2 exhibits the most dispersive low-energy bands, while USb_2 shows the strongest renormalization.

The spectra correspond to the PM DFT+DMFT solution at T = 300 K. The linewidth near E_F therefore reflects both coherent QP weight and finite-temperature scattering, and should not be interpreted directly as a zero-temperature effective mass. The hybridization function discussed above provides a more direct measure of the underlying $5f$–ligand coupling strength.

Under hydrostatic compression [Figs. 3(d–f)], the near-E_F features sharpen and gain spectral weight in all compounds, indicating enhanced QP coherence. The effect is strongest in UP_2, moderate in UAs_2, and weakest in USb_2, consistent with the compound-dependent enhancement of $-\Im[\Delta(\omega)]$ (Fig. 2). The pressure-induced redistribution of spectral weight toward coherent low-energy bands is also consistent with the increase of Z and the enhanced charge fluctuations discussed above.

The momentum dependence further highlights the orbital selectivity of this crossover: the increased coherence under pressure primarily involves the $j = \frac{5}{2}$ manifold, while the $j = \frac{7}{2}$ component remains comparatively incoherent. Enhanced dispersive intensity along Γ–M and Γ–Z reflects an effective bandwidth increase of the $5f$-dominated bands under compression.

In summary, ligand substitution from P to As to Sb reduces the baseline $5f$ itinerancy, whereas hydrostatic pressure enhances QP coherence within each compound. The $\mathbf{k}$-resolved spectra provide direct evidence that the same hybridization trends identified in the local observables manifest as systematic changes in band renormalization and coherence across the UX_2 series.

E. Valence and local-moment diagnostics from DFT+DMFT: $\langle n_{5f}\rangle$ and $\chi_{\rm loc}$

Table II summarizes two complementary DMFT indicators of U–$5f$ localization in the PM phase: the average occupancy $\langle n_{5f}\rangle$ and the local magnetic susceptibility $\chi_{\rm loc}$. Within DMFT,

$$\chi_{\rm loc} = \frac{1}{\beta}\int_0^\beta d\tau\ \langle S_z(\tau)S_z(0)\rangle, \qquad (20)$$

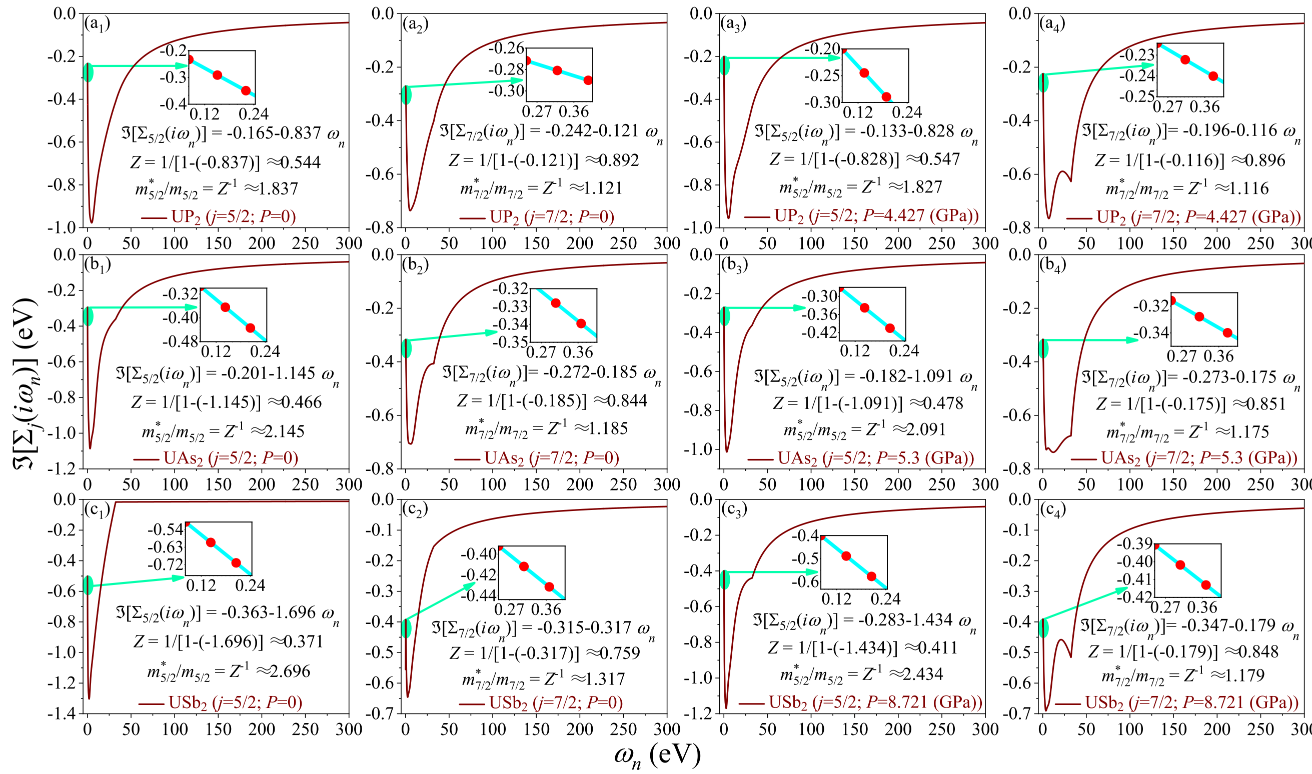

FIG. 4. Imaginary part of the uranium $5f$ self-energy ($\Im[\Sigma_j(i\omega_n)]$) for UX_2 (X = P, As, Sb) obtained from fully charge-self-consistent DFT+DMFT calculations with PBE-GGA including SOC. Panels a_1 and a_3 show $\Im[\Sigma_{5/2}(i\omega_n)]$ of UP_2; b_1 and b_3 show $\Im[\Sigma_{5/2}(i\omega_n)]$ of UAs_2; and c_1 and c_3 show $\Im[\Sigma_{5/2}(i\omega_n)]$ of USb_2. Panels a_2 and a_4 show $\Im[\Sigma_{7/2}(i\omega_n)]$ of UP_2; b_2 and b_4 show $\Im[\Sigma_{7/2}(i\omega_n)]$ of UAs_2; and c_2 and c_4 show $\Im[\Sigma_{7/2}(i\omega_n)]$ of USb_2. Panels a_1, a_2, b_1, b_2, c_1, and c_2 correspond to ambient pressure ($P = 0$), while panels a_3, a_4, b_3, b_4, c_3, and c_4 correspond to hydrostatic compression at P = 4.427, 5.3, and 8.721 GPa for UP_2, UAs_2, and USb_2, respectively. The inset panels enlarge the low-frequency region near $\omega_n \to 0$. The red circles indicate the slope of $\Im[\Sigma_j(i\omega_n)]$ in the Fermi-liquid regime, from which the QP renormalization factor Z is extracted according to Eq. (A3). The corresponding effective mass enhancement follows from Eq. (13).

TABLE II. Average $5f$ occupancy $\langle n_{5f}\rangle$ and local magnetic susceptibility χ_{loc} for PM UX_2 (X = P, As, Sb) from the fully charge self-consistent DFT+DMFT framework using the PBE-GGA functional with SOC.

Compound	P (GPa)	$\langle n_{5f}\rangle$	χ_{loc}
UP_2	0	2.67	61.88
	4.427	2.64	54.26
UAs_2	0	2.73	86.36
	5.300	2.71	75.06
USb_2	0	2.82	125.99
	8.721	2.79	117.22

so χ_{loc} measures the strength of dynamical local-moment (spin) fluctuations on the uranium site.

All three compounds lie in an intermediate-valence regime, with $\langle n_{5f}\rangle$ = 2.64–2.82, i.e., close to but below the nominal $5f^3$ configuration. This is consistent with the mixed $5f^2/5f^3$ character obtained from the valence-state probabilities in Sec. II C. Across the ligand series at ambient pressure, $\langle n_{5f}\rangle$ increases from UP_2 to UAs_2 to USb_2, indicating a progressive shift toward a more localized $5f^3$-like state.

The trend in χ_{loc} is considerably stronger: it rises from 61.88 in UP_2 to 86.36 in UAs_2 and 125.99 in USb_2. This shows that ligand substitution affects dynamical screening more strongly than the average occupancy itself. The increase in χ_{loc} across P→As→Sb is consistent with the reduction of low-energy hybridization discussed above, which suppresses screening, lowers the QP weight, and enhances local-moment character.

Hydrostatic pressure produces the opposite trend within each compound. The occupancy decreases slightly under compression, by about 0.02–0.03, while χ_{loc} is reduced more substantially: by 12.3% in UP_2, 13.1% in UAs_2, and 7.0% in USb_2. The small change in $\langle n_{5f}\rangle$ indicates that pressure does not alter the overall valence regime, but the stronger suppression of χ_{loc} shows that it enhances dynamical screening and weakens local-moment fluctuations.

This behavior is consistent with the pressure dependence of the hybridization function and self-energy. Stronger $5f$–ligand coupling under compression increases screening, enhances the QP weight Z [Eq. (A3)], and reduces the low-frequency slope of $\Im[\Sigma(i\omega_n)]$ in Fig. 4. Together, $\langle n_{5f}\rangle$ and χ_{loc} show that ligand substitution mainly controls the degree of localization across the series, while pressure moderately shifts each compound toward a more coherent and itinerant state.

F. Matsubara self-energy and QP renormalization in UX_2

The imaginary part of the Matsubara self-energy shown in Fig. 4 provides direct access to the QP renormalization factor through Eq. (A3), consistent with the real-frequency definition of the mass enhancement in Eq. (13). The approximately linear approach of $\Im[\Sigma(i\omega_n)]$ toward zero at low Matsubara frequencies confirms that all UX_2 compounds remain in a Fermi-liquid (FL) regime at $T = 300$ K. The slope in this region determines the QP weight Z, while small finite intercepts arise from the finite simulation temperature and statistical noise of the CT-QMC solver.

At ambient pressure, clear orbital differentiation appears between the spin–orbit–split $j = \frac{5}{2}$ and $j = \frac{7}{2}$ manifolds. For the $j = \frac{5}{2}$ states, the QP weights decrease systematically across the series, with $Z \approx 0.54$ for UP_2, 0.47 for UAs_2, and 0.37 for USb_2, corresponding to effective mass enhancements $m^*/m \approx 1.8$, 2.1, and 2.7, respectively. This trend indicates increasing correlation strength from P to As to Sb. In contrast, the $j = \frac{7}{2}$ states remain much less renormalized, with $Z \approx 0.89$, 0.84, and 0.76 for UP_2, UAs_2, and USb_2, respectively, reflecting their more itinerant character. The coexistence of a strongly renormalized $j = \frac{5}{2}$ channel and a weakly renormalized $j = \frac{7}{2}$ channel demonstrates spin–orbit–driven orbital selectivity in the uranium $5f$ shell.

The frequency dependence beyond the linear regime is also consistent with this picture. The larger magnitude and steeper slope of $\Im[\Sigma(i\omega_n)]$ for the $j = \frac{5}{2}$ manifold, particularly in USb_2, indicate stronger dynamical scattering and reduced QP coherence. By contrast, the flatter behavior of the $j = \frac{7}{2}$ component reflects weaker many-body renormalization. No signatures of divergent self-energy behavior associated with a Mott transition are observed, confirming that all compounds remain correlated metals.

Hydrostatic pressure produces a systematic reduction of the low-frequency slope of $\Im[\Sigma(i\omega_n)]$ for both manifolds. Consequently, the QP weights increase and the mass enhancements decrease under compression. This effect is most pronounced in USb_2, where $Z_{5/2}$ increases from approximately 0.37 to 0.41. The pressure dependence therefore indicates enhanced QP coherence driven by stronger $5f$–ligand hybridization, consistent with the pressure evolution of the hybridization function and spectral properties discussed above.

G. Uranium $5f$ valence fluctuations in UX_2 (X = P, As, Sb)

Figure 5 shows the configuration probabilities p_Γ of the uranium $5f$ shell obtained from the CT-QMC impurity solver within the fully charge–self–consistent DFT+DMFT framework. These probabilities quantify the statistical weights of atomic $5f^N$ states and determine the average occupancy $\langle n_{5f}\rangle$ and charge fluctuations through Eq. (9). The resulting valence histograms therefore provide a microscopic view of the dynamical valence fluctuations underlying the spectral properties discussed above.

At ambient pressure [Figs. 5(a–c)], all UX_2 compounds display clear mixed-valence behavior dominated by the $5f^2$ and $5f^3$ configurations. In UP_2, the two configurations carry comparable weights ($\sim$ 47% and $\sim$ 36%, respectively), indicating strong configuration mixing. Across the ligand series P⟶As⟶Sb, the probability distribution shifts toward the $5f^3$ configuration while the $5f^2$ contribution decreases. This systematic redistribution signals a reduction of valence-state mixing and reflects progressively weaker $5f$–ligand hybridization across the series. The trend is consistent with the narrowing of low-energy bands and the reduction of QP weight identified in the spectral and self-energy analyses.

Hydrostatic compression produces the opposite evolution [Figs. 5(d–f)]. Increasing pressure transfers statistical weight from the localized $5f^3$ configuration toward the more itinerant $5f^2$ state. This redistribution indicates enhanced charge fluctuations and stronger dynamical screening, consistent with the pressure-induced increase of QP coherence and hybridization discussed in the previous sections. The small but finite probabilities of $5f^0$, $5f^1$, and $5f^4$ configurations further confirm that the uranium $5f$ shell remains an open quantum subsystem coupled to an itinerant bath.

Taken together, these results show that ligand substitution and hydrostatic pressure tune the $5f$ valence distribution in opposite directions. Substituting P with heavier pnictogens progressively enhances localization by stabilizing the $5f^3$ configuration, whereas hydrostatic compression strengthens hybridization and increases the weight of the more itinerant $5f^2$ state. The ligand-induced redistribution of configuration probabilities is substantially larger than the pressure-driven changes within each compound, indicating that chemical substitution is the dominant control parameter for tuning $5f$ itinerancy in the UX_2 series. The evolution of the configuration histogram therefore provides a microscopic explanation for the corresponding trends observed in the DOS, hybridization function, and QP renormalization.

V. CONCLUSIONS

Fully charge–self–consistent DFT+DMFT calculations including SOC reveal the correlated electronic structure of uranium dipnictides UX_2 (X = P, As, Sb) and provide a unified microscopic description of the dual itinerant–localized character of uranium $5f$ electrons across the series. The calculations primarily consider the experimentally relevant anti–Cu_2Sb ($P4/nmm$) structure in the PM phase at $T = 300$ K.

A comparison with previously reported static AFM DFT calculations provides useful context for the magnetic response of these materials. Earlier zero-temperature DFT studies of the ordered AFM state yield uranium moments of about 1.6–1.9 μ_B, consistent with experimentally observed ordered moments. In contrast, the present finite-temperature DFT+DMFT calculations describe the PM regime and pro-

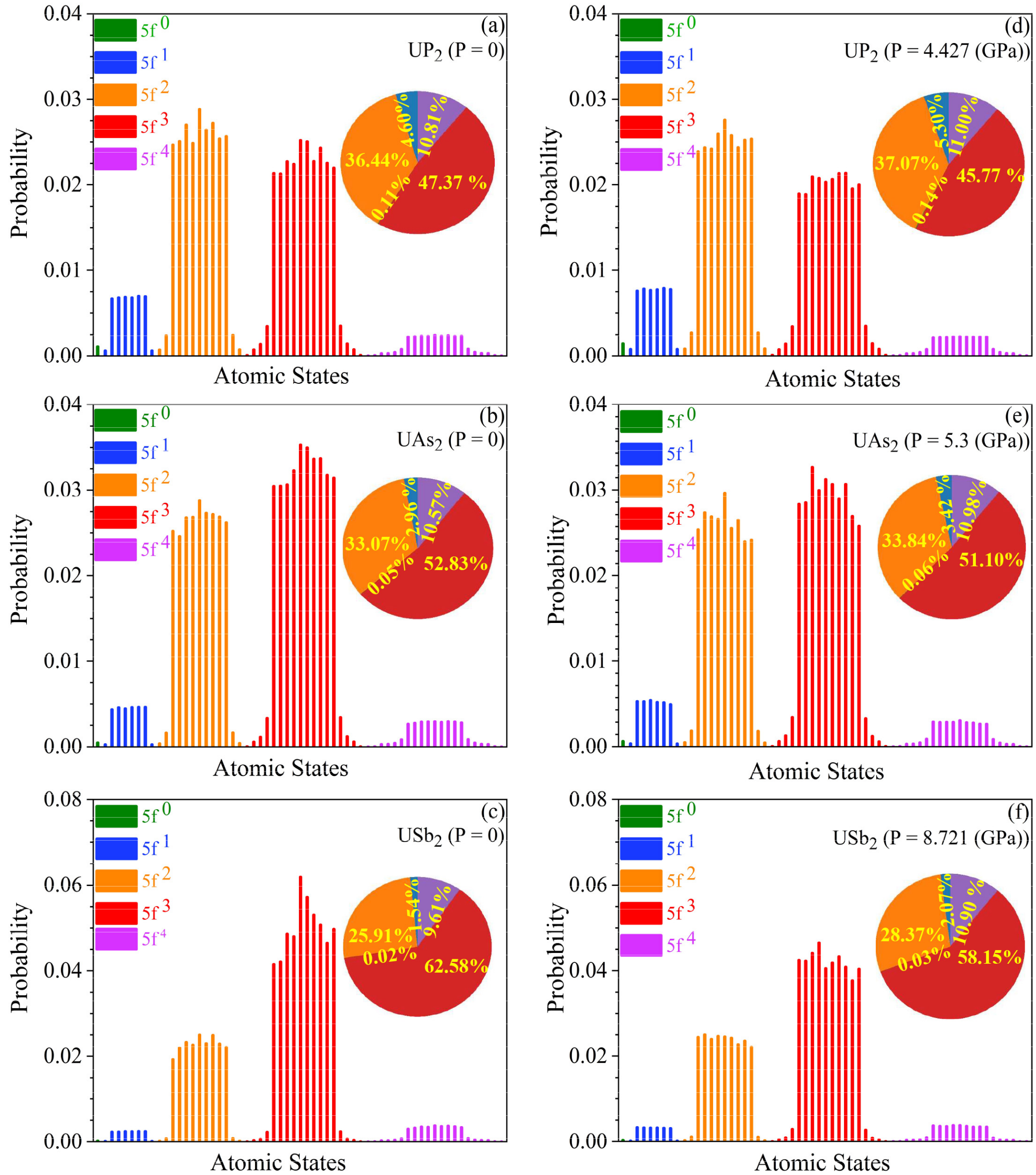

FIG. 5. Visualization of uranium $5f$ atomic-state distributions in UX_2 (X = P, As, Sb) obtained from charge−self−consistent DFT+DMFT calculations including SOC. The bar plots show the statistical probabilities of atomic $5f^N$ configurations ($N = 0$–4) sampled by the CT-QMC impurity solver, while the inset pie charts summarize the corresponding fractional weights for each compound. Panels (a–c) correspond to ambient pressure, and panels (d–f) show hydrostatic compression at P = 4.427, 5.3, and 8.721 GPa for UP_2, UAs_2, and USb_2, respectively. The dominant $5f^2$ and $5f^3$ configurations highlight the mixed-valence nature of uranium in all compounds, while pressure increases the $5f^2$ weight and reduces the $5f^3$ contribution, indicating enhanced itinerancy. The negligible $5f^5$ contribution is omitted for clarity.

duce larger fluctuating local moments of approximately 2.26–2.41 μ_B, arising from thermal fluctuations of the correlated $5f$ shell. The relation between these two regimes can therefore only be discussed qualitatively. It is plausible that the establishment of long-range magnetic order partially suppresses dynamical fluctuations and enhances QP coherence relative to the fluctuation-dominated PM state. A quantitative comparison, however, would require treating the AFM phase within the same DFT+DMFT framework used here for the PM phase so that both regimes are described on an equivalent footing. Within the PM phase studied here, the calculated local moment decreases from UP_2 to USb_2, indicating a systematic evolution of the correlated uranium $5f$ state across the series.

The correlated uranium $5f$ shell exhibits clear signatures of intermediate valence. The calculated occupancies $\langle n_{5f} \rangle \approx$ 2.6–2.8 indicate mixed $5f^2$–$5f^3$ character throughout the UX_2 series. While the occupancy varies only weakly along the ligand sequence P→As→Sb, the local magnetic susceptibility increases substantially, demonstrating that chemical substitution primarily weakens hybridization-driven screening rather than simply transferring charge between atomic configurations. Hydrostatic pressure produces the opposite trend by slightly reducing $\langle n_{5f}\rangle$, enhancing charge fluctuations, and suppressing χ_{loc}, reflecting stronger $5f$–ligand hybridization.

Analysis of the Matsubara self-energy shows that all UX_2 compounds remain coherent FLs at $T = 300$ K while displaying pronounced spin–orbit–driven orbital differentiation. The $j = 5/2$ manifold is substantially more renormalized than the $j = 7/2$ states, yielding a hierarchy of QP weights $Z_{5/2} < Z_{7/2}$, with the renormalization strengthening systematically from UP_2 to USb_2. Hydrostatic compression reduces the slope of the self-energy and increases the QP weight, indicating enhanced itinerancy under pressure. These results demonstrate that electronic correlations in UX_2 are concentrated primarily in the spin–orbit–lowered $j = 5/2$ sector.

These results demonstrate that ligand substitution and hydrostatic compression act as complementary tuning parameters that control a common microscopic quantity—the uranium–ligand hybridization amplitude. Chemical substitution from P to Sb weakens this hybridization and promotes greater $5f$ localization, whereas external pressure enhances hybridization and drives the system toward increased QP coherence. Despite these changes, the UX_2 compounds remain metallic and evolve continuously within a correlated FL regime in which the balance between Coulomb interactions, SOC, and hybridization determines the degree of $5f$ itinerancy.

To assess the structural robustness of this picture, we additionally performed charge–self–consistent DFT+DMFT calculations for UP_2 in its experimentally established tetragonal $I4/mmm$ structure, which contains three inequivalent uranium sites and pronounced crystallographic anisotropy. Although the detailed band dispersions and hybridization strengths differ from those of the simplified $P4/nmm$ description, the essential correlated electronic features remain unchanged. In particular, the low-energy spectrum remains dominated by a spin–orbit–split $5f$ manifold with a strong $j = 5/2$ QP resonance at the E_F, a renormalization hierarchy $Z_{5/2} < Z_{7/2}$, and significant mixed-valence fluctuations between $5f^2$ and $5f^3$ configurations. The response to hydrostatic pressure likewise preserves the trend toward enhanced QP coherence, demonstrating that the hybridization-controlled mechanism governing the localized–itinerant duality of uranium $5f$ electrons is robust with respect to realistic crystallographic refinements.

Overall, these results establish a coherent microscopic picture of the UX_2 series in which chemical substitution and hydrostatic pressure control the balance between localized and itinerant uranium $5f$ states through modifications of the $5f$–ligand hybridization. The UX_2 family therefore provides a representative platform for studying how SOC, electronic correlations, and hybridization cooperate to shape the electronic structure of uranium-based intermetallic compounds.

ACKNOWLEDGEMENTS

This work was carried out as part of the doctoral research of Reyhaneh Ebrahimi-Jaberi under the supervision of S.J-A.

DATA AVAILABILITY

The data supporting the findings of this study are available in the article, its dataset provided in Ref. [61], and its Supplemental Material [43]. Additional data are available from the corresponding author upon reasonable request.

APPENDIX A: Computational Details

This appendix summarizes the technical implementation of the fully charge self-consistent DFT+DMFT calculations used to study UX_2 (X = P, As, Sb). The following subsections detail the DFT setup, the DMFT impurity treatment, and the procedure for simulating hydrostatic pressure.

AI. DFT Setup

The DFT calculations were performed using the full-potential augmented plane-wave plus local orbitals (FP-APW+lo) method as implemented in the WIEN2k code [39]. The exchange–correlation functional was treated within the generalized gradient approximation (PBE-GGA) [42]. SOC was included self-consistently in all calculations.

The experimental lattice parameters reported for UX_2 were used as the initial structural inputs [13, 16, 62]. The initial parameters were $a = 7.200$ Bohr and $c = 14.674$ Bohr for UP_2, $a = 7.473$ Bohr and $c = 15.337$ Bohr for UAs_2, and $a = 8.069$ Bohr and $c = 16.599$ Bohr for USb_2. Starting from these experimental structures, the zero-pressure equilibrium structures were determined using the `2Doptimize` utility in WIEN2k. The optimized lattice parameters and corresponding equilibrium volumes are summarized in Table A1 of Appendix A AII.

The basis expansion employed $l_{\max} = 10$ and $R_{\mathrm{MT}}K_{\max} = 7$, with charge density cutoff $G_{\max} = 14$. Brillouin-zone integrations used an $18\times18\times8$ Monkhorst–Pack grid [52], ensuring total-energy convergence better than 1 meV per atom.

AII. Simulation of Hydrostatic Pressure

Hydrostatic compression was simulated starting from the optimized zero-pressure structures described in Sec. A AI. For each compound, a set of compressed volumes was generated by uniformly scaling the optimized tetragonal unit cell while keeping its zero-pressure c/a ratio fixed. The pressure–volume relation was determined from total-energy calculations combined with an equation-of-state (EOS) analysis. The resulting compressed structures were subsequently used in the paramagnetic DFT+DMFT calculations at $T = 300$ K.

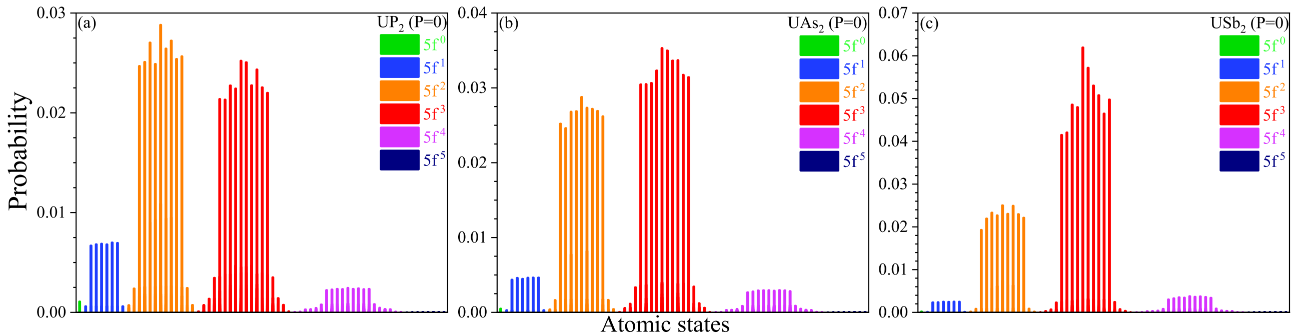

FIG. A1. Atomic-state probability distributions of the uranium $5f$ shell at zero pressure obtained from fully charge–self-consistent DFT+DMFT calculations including SOC for (a) UP_2, (b) UAs_2, and (c) USb_2. The color-coded bars represent the statistical weights of $5f^N$ configurations ($N = 0$–5) sampled by the CT-QMC impurity solver. The dominant $5f^2$–$5f^3$ occupancies reflect the intermediate-valence nature of uranium, while the gradual enhancement of the $5f^3$ weight from UP_2 to USb_2 indicates increasing $5f$ localization and reduced itinerancy with heavier ligands.

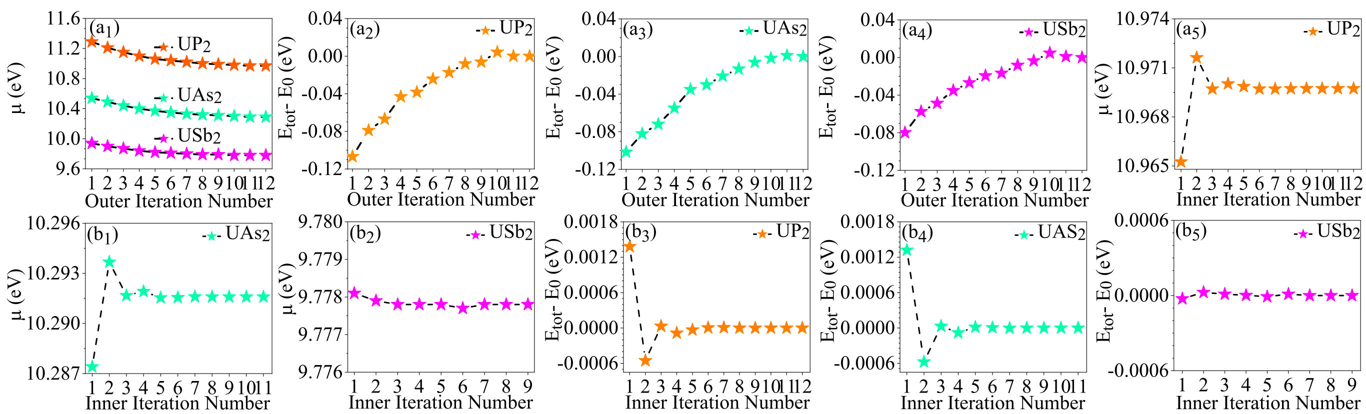

FIG. A2. Convergence of the charge–self–consistent DFT+DMFT calculations using PBE-GGA including SOC at $P = 0$ for UP_2, UAs_2, and USb_2 crystallized in $P4/nmm$ space group. Panels (a$_1$)–(a$_4$) show the evolution of the chemical potential μ and the relative total energy $E_{\rm tot} - E_0$ as functions of the *outer* DFT+DMFT iteration number, where E_0 denotes the final converged total energy. Panels (a$_5$)–(b$_5$) display the corresponding convergence behavior of μ and $E_{\rm tot} - E_0$ within the *inner* DMFT impurity loop evaluated during the maximum outer iteration ($N = 12$). The results demonstrate that the global charge–self–consistent cycle converges after about 8–10 iterations within the adopted total-energy threshold of 10^{-5} Ry, while the embedded impurity loop stabilizes rapidly within only a few iterations.

TABLE A1. EOS-calibrated hydrostatic-pressure points used in the DFT+DMFT calculations for UX_2 (X = P, As, Sb). Here, V_0 is the zero-pressure volume for the indicated method, while V is the sampled volume at pressure P. For the DFT data, the pressure corresponding to each sampled volume was obtained from the Birch–Murnaghan EOS fit, as expressed in Eq. (A1). The relative volume change is defined as $\Delta V/V_0 = (V - V_0)/V_0$. The finite-pressure lattice parameters were reconstructed by keeping the zero-pressure tetragonal ratio c/a fixed. The DFT calculations were performed using the PBE-GGA exchange-correlation functional including SOC. An asterisk denotes the present calculations.

Compound	Method	P (GPa)	V_0 (Bohr^3)	V (Bohr^3)	$\Delta V/V_0$ (%)	a (Bohr)	c (Bohr)	Ref.
UP_2	DFT	0.000	747.038	747.038	0.000	7.176	14.507	*
		4.427	747.038	722.621	−3.269	7.097	14.347	*
	Exp.	0.000	760.700	760.700	0.000	7.200	14.674	[16]
UAs_2	DFT	0.000	850.280	850.280	0.000	7.503	15.104	*
		5.300	850.280	813.452	−4.331	7.393	14.883	*
	Exp.	0.000	856.506	856.506	0.000	7.473	15.337	[16]
USb_2	DFT	0.000	1079.634	1079.634	0.000	8.145	16.274	*
		8.721	1079.634	983.895	−8.868	7.897	15.777	*
	Exp.	0.000	1080.740	1080.740	0.000	8.069	16.599	[13]

The calculated total-energy–volume data were fitted to the third-order Birch–Murnaghan equation of state, from which the pressure at each sampled volume was obtained as

$$P = \frac{3}{2}B_0\left(\eta^7 - \eta^5\right)\left[1 + \frac{3}{4}\left(B_0' - 4\right)\left(\eta^2 - 1\right)\right], \qquad \text{(A1)}$$

where B_0 is the zero-pressure bulk modulus, $B_0' = (\partial B/\partial P)_{P=0}$ is its pressure derivative, $\eta = (V_0/V)^{1/3}$, and V_0 is the calculated zero-pressure equilibrium volume.

The calculated equilibrium and compressed volumes, EOS-derived pressures, reconstructed lattice parameters, and available experimental zero-pressure structural data are summarized in Table A1.

In the computational procedure, a set of compressed volumes was first sampled for each compound, and the corresponding pressures were subsequently determined from the Birch–Murnaghan EOS fit. The pressure values used in the DFT+DMFT calculations are therefore EOS-derived values associated with the sampled volumes rather than independently prescribed target pressures. Their apparently numerical precision results directly from evaluating the fitted EOS at the sampled volumes. The selected points are 4.427 GPa for UP_2, 5.300 GPa for UAs_2, and 8.721 GPa for USb_2, as tabulated in Table A1.

The pressure points were selected according to the compression required to produce clearly discernible changes in the electronic structure of each compound. For UP_2 and UAs_2, the first sampled positive-pressure points already produced identifiable electronic modifications and were therefore retained. In contrast, the more localized U-5f states in USb_2 exhibited a weaker response at the lower sampled compressions, requiring the higher-pressure point of 8.721 GPa to produce comparably discernible changes. The selected points correspond to relative volume changes of −3.269%, −4.331%, and −8.868% for UP_2, UAs_2, and USb_2, respectively. Thus, they represent neither a common applied pressure nor an identical relative volume contraction. The comparison is intended to characterize the compound-dependent electronic response at representative EOS-calibrated compression points rather than to provide a quantitative comparison at identical pressure or strain.

As can be seen from Table A1, the relative deviations of the calculated equilibrium volumes from the corresponding experimental values are approximately −1.80%, −0.73%, and −0.10% for UP_2, UAs_2, and USb_2, respectively. The negative signs indicate that the calculated equilibrium volumes are slightly smaller than the corresponding experimental values. This close agreement supports the reliability of the optimized zero-pressure structures used as reference states in the EOS analysis.

For each sampled volume, the lattice parameters were reconstructed from $V = a^2c = a^3(c/a)$ using the optimized zero-pressure c/a ratio. The resulting lattice parameters were used as structural inputs for the corresponding DFT+DMFT calculations.

AIII. DMFT Implementation, CT-QMC solver, and impurity-basis approximation

The DFT+DMFT calculations were performed using the embedded charge–self-consistent implementation of Refs. [34, 38], interfaced with WIEN2k. The formalism is based on the stationary Luttinger–Ward functional [37] and ensures full charge self-consistency between the DFT and impurity subsystems.

All calculations were carried out at $T = 300$ K in the PM state, corresponding to $\beta = 38.68$ eV^{-1}. The quantum impurity problem was solved using the continuous-time hybridization-expansion CT-QMC method [54–56], with 20×10^6 Monte Carlo steps per DMFT iteration after 3×10^5 thermalization steps.

The local uranium 5f shell was treated in the relativistic $|j, m_j\rangle$ basis by setting `qsplit=4`. This choice separates the one-electron 5f correlated subspace into the $j = 5/2$ and $j = 7/2$ sectors and is appropriate for uranium compounds in the strong spin–orbit-coupling regime. The distinction between the many-electron atomic term symbol, such as $^5L_6$, and the one-electron relativistic $5f_{5/2}$ and $5f_{7/2}$ subspaces used in the DFT+DMFT implementation is discussed in Sec. SMIX of the Supplementary Material. The hierarchy $\lambda_{\mathrm{SOC}} \gg \Delta_{\mathrm{CF}}$ and the corresponding one-electron splitting of the 14-dimensional 5f shell into 6+8 relativistic states are summarized there explicitly.

This relativistic basis also specifies the approximation used in the CT-QMC impurity calculation to control the fermionic sign problem. Instead of solving the impurity problem in a fully unrestricted local-orbital matrix representation, the hybridization function was represented in a symmetry-reduced, relativistic block-structured channel basis. In this representation the dominant spin–orbit structure is incorporated at the level of the correlated subspace, and the independent hybridization channels are organized according to the $j = 5/2$ and $j = 7/2$ sectors. The complete construction of these channels, including the reduction from the matrix-valued DFT+DMFT hybridization to the solver input, is documented in Sec. SMV of the Supplementary Material. In particular, the averaging procedure, the plotted hybridization quantity, and the computational chain connecting `case.dlt1`, `sjoin.py`, `Delta.imp`, `ctqmc.py`, `Delta.inp`, and `ctqmc.cc` are given explicitly there.

Thus, the approximation used here is not an uncontrolled deletion of all off-diagonal matrix elements in an arbitrary orbital basis. Rather, the impurity problem is formulated in a symmetry-adapted relativistic basis in which the hybridization is reduced to independent block-structured channels before being passed to the CT-QMC solver. This is the standard practical strategy used to avoid severe sign instabilities in spin–orbit-coupled multiorbital impurity problems. For the converged calculations reported in this work, the resulting CT-QMC simulations showed an average Monte Carlo sign equal to unity, confirming that the adopted relativistic block-structured representation was numerically stable.

The local Coulomb interaction was set to $U = 4$ eV, with Hund's exchange parameters $J = 0.594$, 0.595, and 0.596 eV for UP_2, UAs_2, and USb_2, respectively. The nominal double-counting correction [34, 57, 58] was employed, with nominal uranium occupancy fixed at $n_f^0 = 3.0$.

Atomic-state probabilities of the uranium $5f$ shell were directly sampled from the CT-QMC impurity solver and are shown in Fig. A1. These probabilities correspond to the statistical weights of the $5f^N$ configurations ($N = 0$–5) contributing to the local many-body density matrix.

Convergence of the charge–self-consistent DFT+DMFT cycle is illustrated in Fig. A2. The outer DFT+DMFT loop converges within 8–10 iterations using a total-energy threshold of 10^{-5} Ry, while the inner impurity loop stabilizes within a few iterations. The converged self-energy was stable to approximately 10^{-4} eV.

After convergence, analytical continuation of the self-energy to the real-frequency axis was performed using the maximum entropy method [50]. The Matsubara-axis hybridization channels were continued in the same manner. More precisely, MEM reconstructs the corresponding real-frequency spectral density by numerically inverting the spectral integral relation given in the Supplementary Material; it is therefore not equivalent to directly replacing $i\omega_n$ by $\omega + i0^+$. Spectral functions were evaluated on a $27 \times 27 \times 13$ k-point mesh.

AIV. Convergence of the Charge–Self–Consistent DFT+DMFT Calculations

Charge–self-consistent DFT+DMFT involves two nested self-consistency cycles: (i) an outer loop updating the lattice charge density and Kohn–Sham potential, and (ii) an inner loop solving the embedded quantum impurity problem to obtain the self-energy $\Sigma(\omega)$ (see Secs. SMII and SMIII of the SM [43]).

Figure A2 summarizes the convergence behavior for UX_2 (X = P, As, Sb) at zero pressure. The outer DFT+DMFT loop shows smooth stabilization of the chemical potential μ and the relative total energy $E_{\rm tot} - E_0$, reaching convergence within approximately 8–10 iterations. Residual energy variations fall below the adopted threshold of 10^{-5} Ry.

The convergence of the inner impurity loop is evaluated during the final outer iteration ($N = 12$). Both μ and $E_{\rm tot} - E_0$ stabilize within a few impurity iterations, indicating rapid convergence of the impurity Green's function and self-energy once the lattice charge density is fixed.

Throughout the calculations, convergence criteria of 10^{-4} e for the total charge and 10^{-5} Ry for the total energy were enforced. Self-consistency between the DFT and DMFT sectors, including charge conservation and projector normalization, was verified at each iteration.

AV. Extraction of the QP weight from the Matsubara self-energy

The QP renormalization factor Z is obtained from the low-frequency behavior of the Matsubara self-energy $\Sigma(i\omega_n)$ computed within the CT-QMC impurity solver. For a FL, the self-energy admits the expansion

$$\Sigma(i\omega_n) \simeq \Sigma(0) + (1 - Z^{-1})\, i\omega_n + O(\omega_n^2), \qquad \text{(A2)}$$

which implies

$$Z = \left[1 - \partial_{\omega_n} \Im[\Sigma(i\omega_n)]\Big|_{\omega_n \to 0}\right]^{-1}. \qquad \text{(A3)}$$

In practice, Z is extracted from a linear fit of $\Im[\Sigma(i\omega_n)]$ using the lowest Matsubara frequencies. The fitting window is restricted to the regime where the self-energy displays linear behavior, ensuring that higher-order ω_n^2 contributions remain negligible. The stability of the extracted Z values is verified by slightly varying the fitting interval.

APPENDIX B: Electronic Structure of UP_2 in the Experimental *I4/mmm* Phase

The UX_2 compounds are often described within the tetragonal anti–Cu_2Sb ($P4/nmm$) structure, which provides a convenient common crystallographic reference for analyzing electronic trends across the series [16, 17, 63]. However, single–crystal diffraction measurements have shown that UP_2 crystallizes in a more complex tetragonal structure with space group $I4/mmm$, containing three inequivalent uranium sites and enlarged lattice parameters [18].

To assess the effect of this structural refinement, we recalculated the electronic structure of UP_2 in the experimental $I4/mmm$ phase using the same fully charge–self–consistent PBE–GGA+DMFT framework described in Sec. II. The following subsections present the corresponding spin–orbit–resolved DOS, hybridization function $-\Im[\Delta(\omega)]$, Matsubara self-energies (Fig. B1), momentum-resolved spectral function $A(\mathbf{k}, \omega)$, and CT-QMC valence statistics (Fig. B2).

The results show that the main electronic features identified in the $P4/nmm$ calculations—SOC splitting of the $5f$ states, dominance of the $j = 5/2$ manifold near E_F, and pressure-enhanced QP coherence—remain robust in the experimental $I4/mmm$ structure.

BI. Spectral Structure, Spin–Orbit Hybridization, and QP Coherence in in UP_2 (*I4/mmm*) under Pressure

Figure B1 summarizes the correlated electronic structure of UP_2 in the tetragonal $I4/mmm$ phase obtained from fully charge–self–consistent DFT+DMFT calculations including SOC. The interacting DOS derived from the lattice Green's function shows that the low-energy electronic structure is dominated by uranium $5f$ states, while the phosphorus p orbitals occupy mainly the deeper valence region between approximately -4 and -0.5 eV [Fig. B1(a_1)]. The SOC-resolved spectrum [Fig. B1(a_2)] separates the $5f$ shell into $j = 5/2$ and $j = 7/2$ manifolds, with the $j = 5/2$ component providing the dominant spectral weight near the E_F.

Hydrostatic compression ($P = 4.427$ GPa) produces a moderate redistribution of spectral weight around E_F while

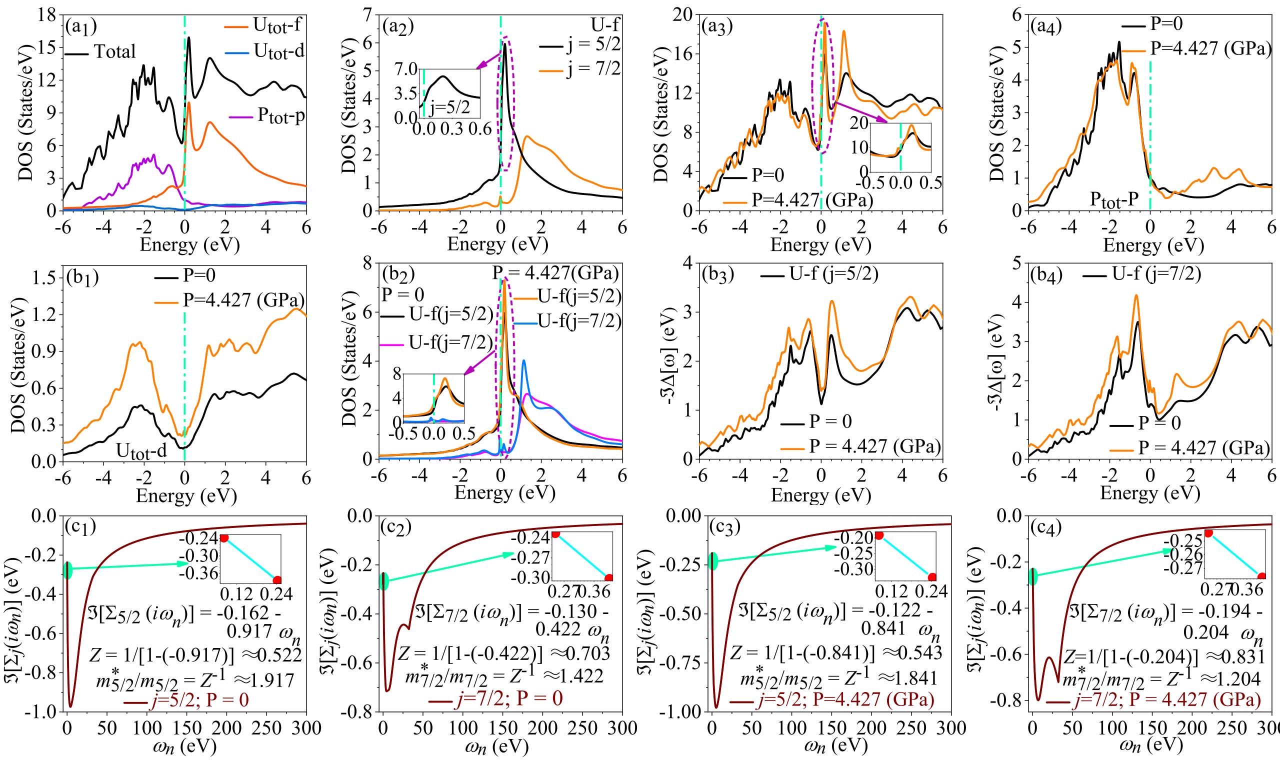

FIG. B1. Correlated electronic structure of UP_2 in the $I4/mmm$ phase obtained from DFT+DMFT using PBE-GGA and including SOC. The interacting DOS is computed from the lattice Green's function [Eq. (5)] and $A(\mathbf{k},\omega)$ [Eq. (7)]. (a_1) Total and orbital-resolved DOS at ambient pressure. (a_2) SOC-resolved U $5f$ states showing the $j = 5/2$ and $j = 7/2$ manifolds. (a_3) Total DOS at $P = 0$ and under hydrostatic compression ($P = 4.427$ GPa). (a_4) Pressure evolution of ligand p states. (b_1) Projected DOS of U d orbitals. (b_2) Pressure-dependent redistribution of spectral weight in the U $5f$ manifold, resolving the $j = 5/2$ and $j = 7/2$ components (inset highlights the low-energy region near the E_F). (b_3)–(b_4) Hybridization spectra $-\Im[\Delta(\omega)]$ for the $j = 5/2$ and $j = 7/2$ $5f$ states, defined from the impurity Dyson equation [Eq. (2)] and embedding relation [Eq. (4)]. Black and orange curves correspond to $P = 0$ and $P = 4.427$ GPa. (c_1)–(c_4) Imaginary part of the Matsubara self-energy $\Im[\Sigma_j(i\omega_n)]$ for the $j = 5/2$ and $j = 7/2$ manifolds at $P = 0$ and $P = 4.427$ GPa. Insets enlarge the low-frequency region near $\omega_n \to 0$. Red circles indicate the linear FL regime used to extract the QP weight Z via Eq. (A3) [see also Eq. (13)]. The vertical dash-dotted line marks the E_F.

preserving the overall metallic character of the system [Fig. B1(a_3)]. A small increase of ligand p spectral weight near the E_F [Fig. B1(a_4)] indicates enhanced $5f$–p hybridization as the U–P bond length decreases under pressure. The projected spectra in Figs. B1(b_1)–(b_2) further show that the low-energy QP feature originates primarily from the $j = 5/2$ manifold, whereas the $j = 7/2$ states remain mostly at higher excitation energies.

The hybridization spectra $-\Im[\Delta(\omega)]$ [Figs. B1(b_3)–(b_4)] reveal that the $j = 5/2$ channel couples more strongly to the conduction bath near the E_F. Under compression the overall hybridization amplitude increases for both spin–orbit components, reflecting enhanced orbital overlap between uranium and ligand states.

Dynamical correlation effects are illustrated by the Matsubara self-energies $\Im[\Sigma_j(i\omega_n)]$ in Figs. B1(c_1)–(c_4). Both spin–orbit manifolds display a linear low-frequency behavior characteristic of a FL. The extracted QP weights are $Z_{5/2} \approx 0.52$ and $Z_{7/2} \approx 0.70$ at ambient pressure, corresponding to moderate mass renormalizations. Under hydrostatic compression these values increase slightly ($Z_{5/2} \approx 0.54$, $Z_{7/2} \approx 0.83$), indicating enhanced QP coherence driven by stronger hybridization.

Overall, the calculations confirm that UP_2 in the experimental $I4/mmm$ structure remains a moderately correlated spin–orbit–selective FL. The low-energy electronic structure is governed by the $j = 5/2$ manifold, and hydrostatic pressure primarily enhances hybridization and QP coherence without altering the fundamental SOC-induced hierarchy of the $5f$ states.

BII. QP coherence, mixed-valence fluctuations, and dynamical local moments in UP_2 (*I4/mmm*)

Figure B2 shows the momentum-resolved spectral function $A(\mathbf{k},\omega)$ and the CT-QMC valence histograms for UP_2 in the tetragonal $I4/mmm$ phase obtained from fully charge-self-consistent PBE-GGA+DMFT calculations including SOC.

The spectral function at ambient pressure [Fig. B2(a)] exhibits several dispersive bands crossing the E_F along Γ–X–M–Γ–Z–R–A–M–Γ, confirming the metallic character of the

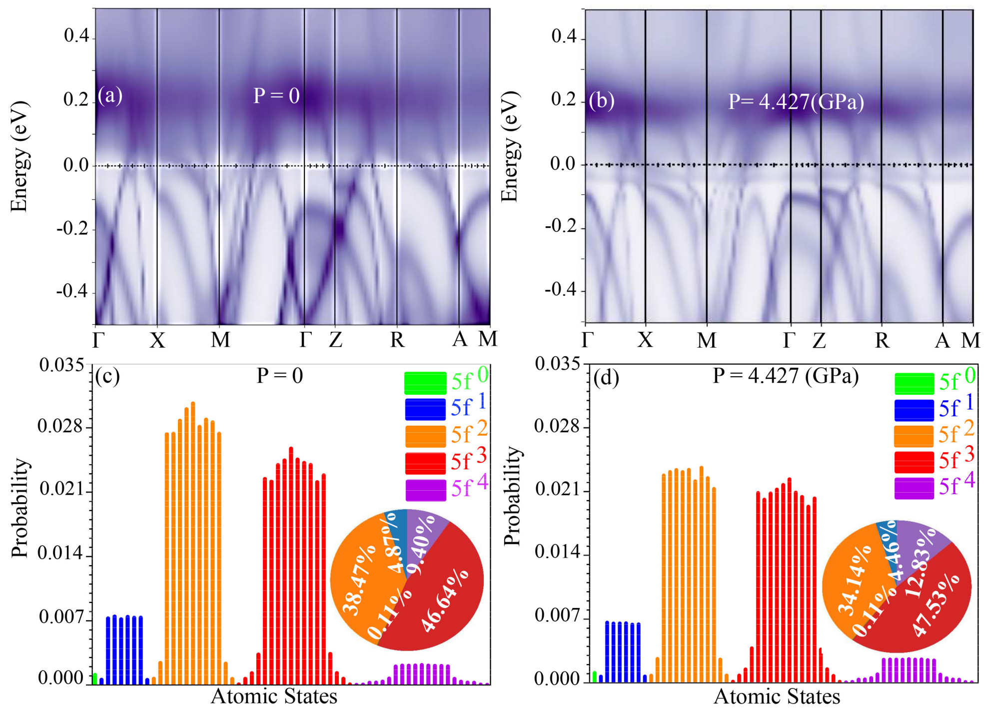

FIG. B2. (a,b) Momentum-resolved spectral function $A(\mathbf{k},\omega)$ of UP_2 in the tetragonal $I4/mmm$ phase from the interacting lattice Green's function [Eq. (5)] using Eq. (7) at (a) $P = 0$ and (b) $P = 4.427$ GPa. Spectra are shown along Γ–X–M–Γ–Z–R–A–M–Γ; the dashed line marks E_F. SOC splits the U $5f$ manifold into $j = \frac{5}{2}$ and $j = \frac{7}{2}$ states, with $j = \frac{5}{2}$ dominating near E_F. (c,d) CT-QMC valence histograms for the U $5f$ shell at (c) $P = 0$ and (d) $P = 4.427$ GPa within charge-self-consistent PBE-GGA+DMFT including SOC. Bars show probabilities p_Γ of $5f^N$ configurations ($N = 0$–4), determining occupancy and charge fluctuations via Eq. (9). Dominant $5f^2$ and $5f^3$ weights indicate mixed valence.

system. The low-energy spectral weight is dominated by uranium $5f$ states forming narrow QP bands near E_F. Strong SOC splits the $5f$ manifold into $j = \frac{5}{2}$ and $j = \frac{7}{2}$ components, with the $j = \frac{5}{2}$ states providing the dominant contribution to the QP bands while the $j = \frac{7}{2}$ states appear mainly at higher excitation energies. Under hydrostatic compression ($P = 4.427$ GPa) the near-E_F bands become slightly sharper and more dispersive [Fig. B2(b)], indicating enhanced QP coherence and stronger $5f$–ligand hybridization.

The CT-QMC valence histograms shown in Figs. B2(c,d) reveal a clear intermediate-valence character dominated by $5f^2$ and $5f^3$ configurations. At ambient pressure the corresponding probabilities are approximately 38.5% ($5f^2$) and 46.6% ($5f^3$), while smaller $5f^1$ and $5f^4$ contributions reflect residual charge fluctuations between the $5f$ shell and the conduction bath. Under compression the relative weights change only slightly, indicating that pressure mainly affects hybridization and QP coherence rather than the overall valence state.

Additional thermodynamic diagnostics are summarized in Table B1. At ambient pressure the average occupancy $\langle n_{5f}\rangle = 2.62$ and the local susceptibility $\chi_{\rm loc} = 65.19$ confirm an intermediate-valence regime with sizable dynamical local-moment fluctuations. These values are very close to those obtained for the $P4/nmm$ structure, demonstrating that the balance between localized and itinerant $5f$ behavior is only weakly affected by the structural description.

Under hydrostatic compression the occupancy increases slightly to $\langle n_{5f}\rangle = 2.71$, whereas the local susceptibility decreases to $\chi_{\rm loc} = 52.75$. The stronger pressure dependence of $\chi_{\rm loc}$ reflects enhanced dynamical screening of the uranium $5f$ moments due to increased hybridization with conduction states. Consistently, the fluctuating local moment is calculated to be $\mu_{\rm U} = 2.361\,\mu_{\rm B}$, in close agreement with both the $P4/nmm$ DFT+DMFT result and the experimental Curie–Weiss value $\mu_{\rm U} \approx 2.50\,\mu_{\rm B}$ [16].

TABLE B1. Average $5f$ occupancy $\langle n_{5f}\rangle$ and local magnetic susceptibility $\chi_{\rm loc}$ for PM UP_2 in the tetragonal $I4/mmm$ structure obtained from fully charge self-consistent DFT+DMFT calculations using the PBE-GGA functional including SOC.

Compound	P (GPa)	$\langle n_{5f}\rangle$	$\chi_{\rm loc}$
UP_2	0	2.62	65.19
	4.427	2.71	52.75

Overall, the spectral, statistical, and thermodynamic diagnostics consistently show that UP_2 in the experimental $I4/mmm$ structure remains a moderately correlated intermediate-valence system. The low-energy electronic structure is governed by the SOC-split uranium $5f$ manifold, with the $j = \frac{5}{2}$ states dominating the QP bands. Hydrostatic pressure primarily enhances $5f$–ligand hybridization, increases QP coherence, and suppresses dynamical local-moment fluctuations without qualitatively changing the mixed-valence character of the $5f$ shell.

---

[1] J. L. Sarrao, L. A. Morales, J. D. Thompson, B. L. Scott, G. R. Stewart, F. Wastin, J. Rebizant, P. Boulet, E. Colineau, and G. H. Lander, Plutonium-based superconductivity with a transition temperature above 18 K, Nature **420**, 297 (2002).

[2] Y. Ōnuki, Y. Haga, E. Yamamoto, Y. Inada, R. Settai, H. Yamagami, and H. Harima, High-quality single crystal growth and the Fermi surface property of uranium and cerium compounds, J. Phys.: Condens. Matter **15**, S1903 (2003).

[3] Y. Ōnuki, R. Settai, H. Shishido, S. Ikeda, T. Matsuda, E. Yamamoto, Y. Haga, D. Aoki, H. Harima, and H. Yamagami, Fermi surface properties and unconventional superconductivity in rare earth, uranium and transuranium compounds, J. Optoelectron. Adv. Mater. **10**, 1535 (2008).

[4] R. Wawryk, J. Mucha, H. Misiorek, and Z. Henkie, Thermal conductivity of USb_2 and UBi_2 single crystals, Philos. Mag. **90**, 793 (2010).

[5] P. G. Pagliuso, N. O. Moreno, N. J. Curro, J. D. Thompson, M. F. Hundley, J. L. Sarrao, Z. Fisk, A. D. Christianson, A. H. Lacerda, B. E. Light, and A. L. Cornelius, Ce-site dilution studies in the antiferromagnetic heavy fermions $Ce_mRh_nIn_{3m+2n}$ ($m = 1, 2; n = 0, 1$), Phys. Rev. B **66**, 054433 (2002).

[6] Y. Ōnuki, D. Aokit, P. Wiśniewski, H. Shishido, S. Ikeda, Y. Inada, R. Settai, Y. Tokiwa, E. Yamamoto, Y. Haga, *et al.*, Quasi-two dimensional fermi surfaces in rare earth and uranium compounds: UX_2 , $CeTIn_5$ and $UTGa_5$, Acta Phys. Pol. B **32**, 3273 (2001).

[7] G. R. Stewart, Non-Fermi-liquid behavior in d- and f-electron metals, Rev. Mod. Phys. **73**, 797 (2001).

[8] S. Lebègue, P. M. Oppeneer, and O. Eriksson, Ab initio study of the electronic properties and Fermi surface of the uranium dipnictides, Phys. Rev. B **73**, 045119 (2006).

[9] K. T. Moore and G. van der Laan, Nature of the $5f$ states in actinide metals, Rev. Mod. Phys. **81**, 235 (2009).

[10] G. R. Stewart, Heavy-fermion systems, Rev. Mod. Phys. **56**, 755 (1984).

[11] D. Aoki, P. Wiśniewski, K. Miyake, N. Watanabe, Y. Inada, R. Settai, E. Yamamoto, Y. Haga, and Y. Onuki, Cylindrical Fermi surfaces formed by a fiat magnetic Brillouin zone in uranium dipnictides, Philos. Mag. B **80**, 1517 (2000).

[12] D. Aoki, P. Wiśniewski, K. Miyake, N. Watanabe, Y. Inada, R. Settai, E. Yamamoto, Y. Haga, and Y. Onuki, Crystal growth and cylindrical Fermi surfaces of USb_2, J. Phys. Soc. Jpn. **68**, 2182 (1999).

[13] E. Guziewicz, T. Durakiewicz, M. T. Butterfield, C. G. Olson, J. J. Joyce, A. J. Arko, J. L. Sarrao, D. P. Moore, and L. Morales, Angle-resolved photoemission study of USb_2 : The $5f$ band structure, Phys. Rev. B **69**, 045102 (2004).

[14] S. Tsutsui, M. Nakada, S. Nasu, Y. Haga, D. Aoki, P. Wiśniewski, and Y. Ōnuki, Hyperfine interactions in the antiferromagnetic states of UX_2 (X = P, As, Sb, Bi), Phys. Rev. B **69**, 054404 (2004).

[15] F. Grønvold, M. R. Zaki, E. F. Westrum, J. A. Sommers, and D. B. Downie, Actinoid pnictides—II: Heat capacities of UAs_2 and USb_2 from 5 to 750 K and antiferromagnetic transitions, J. Inorg. Nucl. Chem. **40**, 635 (1978).

[16] G. Amoretti, A. Blaise, and J. Mulak, Crystal field interpretation of the magnetic properties of UX_2 compounds (X = P, As, Sb, Bi), J. Magn. Magn. Mater. **42**, 65 (1984).

[17] Z. Henkie, P. Wiśniewski, R. Fabrowski, and R. Maślanka, Dependence of ordering temperature on pressure, carrier density and U-U distance in uranium pnictides; pressure and hall effects examinations of UP_2 and USb_2, Solid State Commun. **79**, 1025 (1991).

[18] P. Wiśniewski, D. Aoki, N. Watanabe, R. Settai, Y. Haga, E. Yamamoto, and Y. Ōnuki, Shubnikov–de haas effect study of cylindrical fermi surfaces in UP_2, J. Phys. Soc. Jpn. **70**, 278 (2001).

[19] Z. Henkie and P. Markowski, Crystal growth of uranium and thorium compounds with the elements of group V by chemical vapor transport, J. Cryst. Growth. **41**, 303 (1977).

[20] S. Chen, M. Hawley, P. V. Stockum, H. Manoharan, and E. Bauer, Surface structure of cleaved (001) USb_2 single crystal, Philos. Mag. **89**, 1881 (2009).

[21] Z. Henkie and W. Trzebiatowski, Electrical properties of monocrystalline uranium diphosphide, Phys. Status Solidi B **35**, 827 (1969).

[22] M. M. Wysokiński, Microscopic mechanism for the unusual antiferromagnetic order and the pressure-induced transition to ferromagnetism in USb_2, Phys. Rev. B **97**, 041107 (2018).

[23] H. ADACHI and S. IMOTO, Magnetic susceptibility and electrical resistivity of uranium phosphides and UP-ThP solid solutions, J. Nucl. Sci. Technol. **6**, 531 (1969).

[24] R. L. Stillwell, I.-L. Liu, N. Harrison, M. Jaime, J. R. Jeffries, and N. P. Butch, Tricritical point of the f-electron antiferromagnet USb_2 driven by high magnetic fields, Phys. Rev. B **95**, 014414 (2017).

[25] J. R. Jeffries, R. L. Stillwell, S. T. Weir, Y. K. Vohra, and N. P. Butch, Emergent ferromagnetism and T-linear scattering in USb_2 at high pressure, Phys. Rev. B **93**, 184406 (2016).

[26] R. Wawryk, Magnetic and transport properties of UBi_2 and USb_2 single crystals, Philos. Mag. **86**, 1775 (2006).

[27] F. Friedman, J. Grunzweig, and M. Kuznietz, Knigth shift of 31p NMR in the paramagnetic state of uranium phosphides, Phys. Lett. A **25**, 690 (1967).

[28] K. Easwaran, V. S. Rao, R. Vijayaraghavan, and U. Rao, Nuclear magnetic resonance of 31p in the paramagnetic state of UP_2, Phys. Lett. A **25**, 683 (1967).

[29] P. Wiśniewski, D. Aoki, K. Miyake, N. Watanabe, Y. Inada, R. Settai, Y. Haga, E. Yamamoto, and Y. Ōnuki, Cylindrical Fermi surfaces of UAs_2 and UP_2, Phys. B **281-282**, 769 (2000).

[30] Z. Henkie, R. Maślanka, P. Wiśniewski, R. Fabrowski, P. Markowski, J. Franse, and M. van Sprang, Anisotropy of the physical properties of uniaxial antiferromagnetic USb_2, J. Alloy. Compd. **181**, 267 (1992), proceedings of the 19th Rare Earth Research Conference.

[31] S. Lebègue, P. M. Oppeneer, and O. Eriksson, Ab initio study of the electronic properties and Fermi surface of the uranium dipnictides, Phys. Rev. B **73**, 045119 (2006).

[32] E. Ghasemikhah, S. Jalali Asadabadi, I. Ahmad, and M. Yazdani-Kacoei, Ab initio studies of electric field gradients and magnetic properties of uranium dipnicties, Rsc Adv. **5**, 37592 (2015).

[33] V. I. Anisimov, J. Zaanen, and O. K. Andersen, Band theory and Mott insulators: Hubbard U instead of Stoner I, Phys. Rev. B **44**, 943 (1991).

[34] K. Haule, Exact double counting in combining the dynamical mean field theory and the density functional theory, Phys. Rev. Lett. **115**, 196403 (2015).

[35] A. Georges, G. Kotliar, W. Krauth, and M. J. Rozenberg, Dynamical mean-field theory of strongly correlated fermion systems and the limit of infinite dimensions, Rev. Mod. Phys. **68**, 13 (1996).

[36] G. Kotliar, S. Y. Savrasov, K. Haule, V. S. Oudovenko, O. Parcollet, and C. A. Marianetti, Electronic structure calculations with dynamical mean-field theory, Rev. Mod. Phys. **78**, 865 (2006).

[37] K. Haule and T. Birol, Free energy from stationary implementation of the DFT+DMFT functional, Phys. Rev. Lett. **115**, 256402 (2015).

[38] K. Haule, Structural predictions for correlated electron materials using the functional dynamical mean field theory approach, J. Phys. Soc. Jpn. **87**, 041005 (2018).

[39] P. Blaha, K. Schwarz, F. Tran, R. Laskowski, G. K. H. Madsen, and L. D. Marks, WIEN2k: An APW+lo program for calculating the properties of solids, J. Chem. Phys. **152**, 074101 (2020), https://doi.org/10.1063/1.5143061.

[40] P. Hohenberg and W. Kohn, Inhomogeneous electron gas, Phys. Rev. **136**, B864 (1964).

[41] W. Kohn and L. J. Sham, Self-consistent equations including exchange and correlation effects, Phys. Rev. **140**, A1133 (1965).

[42] J. P. Perdew, K. Burke, and M. Ernzerhof, Generalized gradient approximation made simple, Phys. Rev. Lett. **77**, 3865 (1996).

[43] R. Ebrahimi-Jaberi and S. Jalali-Asadabadi, Supplemental Material (SM): Microscopic Mechanisms and Dual Pathways of 5f Electron Itinerancy Tuned by Ligand Chemistry and Pressure in Paramagnetic Uranium Dipnictides (2026), Convergence and validation of DFT+DMFT calculations, with extended electronic-structure analysis of UP_2 in $I4/mm$ phase at $T = 300$ K under pressure. Includes DOS, $-\Im[\Delta(\omega)]$, $A(\mathbf{k},\omega)$, $\Im[\Sigma_j(i\omega_n)]$, quasiparticle renormalization, valence-state probabilities, and thermodynamic observables. URL: `https://link.aps.org/doi/x.x/PhysRevB.x.x`.

[44] R. Ebrahimi-Jaberi and S. Jalali-Asadabadi, Anisotropic mechanical behavior and thermal attributes of antiferromagnetic UX_2(X = P, As, Sb) materials: A density functional and elasticity theories study, Mater. Chem. Phys. **312**, 128590 (2024).

[45] A. Östlin, L. Vitos, and L. Chioncel, Analytic continuation-free green's function approach to correlated electronic structure calculations, Phys. Rev. B **96**, 125156 (2017).

[46] M. Aichhorn, L. Pourovskii, P. Seth, V. Vildosola, M. Zingl, O. E. Peil, X. Deng, J. Mravlje, G. J. Kraberger, C. Martins, M. Ferrero, and O. Parcollet, Triqs/dfttools: A triqs application for ab initio calculations of correlated materials, Comput. Phys. Commun. **204**, 200 (2016).

[47] A. Grechnev, I. Di Marco, M. I. Katsnelson, A. I. Lichtenstein, J. Wills, and O. Eriksson, Theory of bulk and surface quasiparticle spectra for fe, co, and ni, Phys. Rev. B **76**, 035107 (2007).

[48] J.-M. Wang, J.-X. Wang, R.-Q. He, L. Huang, and Z.-Y. Lu, Ab initio dynamical mean field theory with natural orbitals renormalization group impurity solver, Npj Comput. Mater. **11**, 86 (2025).

[49] J. Li and T. Zhu, Restoring translational symmetry in periodic all-orbital dynamical mean-field theory simulations, Faraday Discuss. **254**, 641 (2024).

[50] M. Jarrell and J. Gubernatis, Bayesian inference and the analytic continuation of imaginary-time quantum Monte Carlo data, Phys. Rep. **269**, 133 (1996).

[51] G. K. H. Madsen, P. Blaha, K. Schwarz, E. Sjöstedt, and L. Nordström, Efficient linearization of the augmented plane-wave method, Phys. Rev. B **64**, 195134 (2001).

[52] H. J. Monkhorst and J. D. Pack, Special points for Brillouin-zone integrations, Phys. Rev. B **13**, 5188 (1976).

[53] P. Blaha, K. Schwarz, G. K. Madsen, D. Kvasnicka, J. Luitz, *et al.*, wien2k, User Guide **60** (2001).

[54] K. Haule, Quantum Monte Carlo impurity solver for cluster dynamical mean-field theory and electronic structure calculations with adjustable cluster base, Phys. Rev. B **75**, 155113 (2007).

[55] P. Werner, A. Comanac, L. de' Medici, M. Troyer, and A. J. Millis, Continuous-time solver for quantum impurity models, Phys. Rev. Lett. **97**, 076405 (2006).

[56] P. Sémon, C.-H. Yee, K. Haule, and A.-M. S. Tremblay, Lazy skip-lists: An algorithm for fast hybridization-expansion quantum Monte Carlo, Phys. Rev. B **90**, 075149 (2014).

[57] K. Haule, C.-H. Yee, and K. Kim, Dynamical mean-field theory within the full-potential methods: Electronic structure of $CeIrIn_5$, $CeCoIn_5$, and $CeRhIn_5$, Phys. Rev. B **81**, 195107 (2010).

[58] K. Haule, T. Birol, and G. Kotliar, Covalency in transition-metal oxides within all-electron dynamical mean-field theory, Phys. Rev. B **90**, 075136 (2014).

[59] T. Katsura and Y. Tange, A simple derivation of the Birch–Murnaghan equations of state (EOSs) and comparison with EOSs derived from other definitions of finite strain, Minerals **9**, 10.3390/min9120745 (2019).

[60] L. Mollabashi, S. Jalali-Asadabadi, C. Rudowicz, M. Acikgoz, Z. Ghasemi-Dorcheh, R. Ebrahimi-Jaberi, M. Jalali-Asadabadi, S. Rahimi, and F. Jalali-Asadabadi, Numerical study of the temperature-dependent magnetization and susceptibility of tm^{3+} in $litmf_4$, Phys. Rev. B **110**, 054440 (2024).

[61] R. Ebrahimi-Jaberi and S. Jalali-Asadabadi, Supplementary Dataset and Computational Details Supporting the Main Article Entitled: Microscopic Mechanisms and Dual Pathways of 5f Electron Itinerancy Tuned by Ligand Chemistry and Pressure in Paramagnetic Uranium Dipnictides (2026), DFT+DMFT results in UX_2 at $T = 300$ K under ligand substitution and pressure. Includes DOS, hybridization $-\Im[\Delta(\omega)]$, spectral functions $A(\mathbf{k},\omega)$, $5f$ atomic-state probabilities, and Matsubara self-energies $\Im[\Sigma_j(i\omega_n)]$ for $j = 5/2, 7/2$. URL: `https://doi.org/10.6084/m9.figshare.31967763`; README: `https://figshare.com/ndownloader/files/67557054`.

[62] F. Friedman, J. Grunzweig, and M. Kuznietz, Knigth shift of 31p NMR in the paramagnetic state of uranium phosphides, Phys. Lett. A **25**, 690 (1967).

[63] Y. Jiang, Z. Song, T. Zhu, Z. Fang, H. Weng, Z.-X. Liu, J. Yang, and C. Fang, Enumeration of spin-space groups: Toward a complete description of symmetries of magnetic orders, Phys. Rev. X **14**, 031039 (2024).